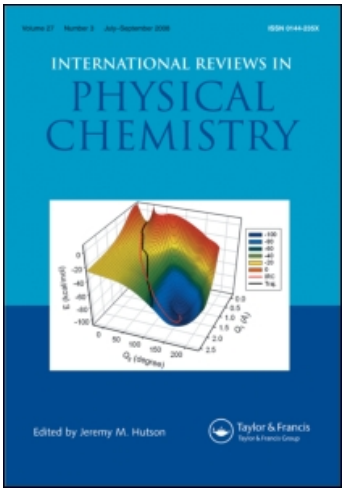

International Reviews in Physical Chemistry
Publication details, including instructions for authors and subscription information:
http://www.informaworld.com/smpp/title~content=t713724383

Spectroscopy and chemical dynamics of weakly bound alkaline-earth metal ion-H and alkaline-earth metal ion-hydrocarbon complexes 2

Paul D. Kleiber; Jing Chen

Online publication date: 26 November 2010

To cite this Article Kleiber, Paul D. and Chen, Jing(1998) 'Spectroscopy and chemical dynamics of weakly bound alkaline-earth metal ion-H and alkaline-earth metal ion-hydrocarbon complexes 2', International Reviews in Physical Chemistry, 17: 1, 1 — 34
To link to this Article: DOI: 10.1080/014423598230153
URL: http://dx.doi.org/10.1080/014423598230153

INTERNATIONAL REVIEWS IN PHYSICAL CHEMISTRY, 1998, VOL. 17, NO. 1, 1–34

Spectroscopy and chemical dynamics of weakly bound alkaline-earth metal ion–H_2 and alkaline-earth metal ion–hydrocarbon complexes

by PAUL D. KLEIBER and JING CHEN

Department of Physics and Astronomy, University of Iowa, Iowa City, IA 52242, USA

The activation of hydrocarbon bonds by metal atoms are among the most vital processes in chemistry. This review focuses on the spectroscopy and chemical dynamics of weakly bound alkaline-earth metal ion–H_2 and alkaline-earth metal ion–hydrocarbon bimolecular complexes using mass-resolved photodissociation spectroscopy techniques. The photodissociation spectroscopy of isolated clusters, in concert with translational energy spectroscopy of the products, gives unique and detailed insight into the fundamental metal–hydrocarbon interactions. Measurements of the product yield, translational energy release and photofragment anisotropy as a function of the photolysis laser wavelength give quantitative information about the structure, lifetime and bonding of the complex and insight into the nuclear motion dynamics and the electronic non-adiabatic interactions which determine the product branching and energy partitioning. The experimental techniques of photodissociation spectroscopy are reviewed. Several examples are discussed including examples of the photoactivation of H–H and C–H σ bonds and of C=C π bonds by Mg^+. In each case, a strong electronic orbital alignment selectivity is observed. The quenching mechanism can be explained by a bond-stretch process leading to rapid but non-adiabatic dissociation of the complex through a conical intersection or narrowly avoided surface crossing with the ground electronic surface. Additional examples of the photoactivation of C–O bonds and of photoinduced charge transfer chemistry are also discussed

1. Introduction

The photodissociation of a weakly bound 'precursor' complex can serve to mimic a bimolecular 'half-collision' and represents an especially fruitful experimental approach to the study of molecular dynamics [1–41]. In many cases the structure of the precursor complex can be determined through either *ab-initio* calculation or through bound-state spectroscopy. Following absorption, the subsequent half-collision begins from a well defined geometry and electronic orbital alignment, and with a restricted range of collision energies and relative angular momenta. Measurement of the product yield, internal quantum state distribution, translational energy release and photofragment anisotropy as functions of the photolysis laser wavelength can give information about the structure and lifetime of the complex, and the dynamical effects which determine the energy partitioning and competitive branching in multichannel processes. These experiments can give insight into the nuclear motion dynamics, stereochemical effects and the electronic non-adiabatic interactions which couple the adiabatic Born–Oppenheimer potential energy surfaces.

The coupling of supersonic molecular beam sources with laser spectroscopy techniques has allowed experimenters to probe in detail the structure and dynamics of a variety of interesting and important weakly bound molecular clusters by photodissociation spectroscopy, including both neutral van der Waals complexes and electrostatically bound ion–molecule complexes [1–41].

Ion–molecule complexes are generally more strongly bound by ion–multiple

0144–235X/98 $12.00

electrostatic forces than are their neutral counterparts. Binding energies typically lie in the approximate range 0.1–1 eV, intermediate between the very weak van der Waals limit and the limit of true chemical bonding. As a result, ion–molecule complexes can be easier to generate and will typically have a more rigid and well characterized structure than neutral van der Waals complexes (which can be quite floppy). This can simplify the interpretation of the subsequent dissociation dynamics by restricting the average over initial geometries. Furthermore, using tandem mass spectrometry (MS–MS) techniques, the mass of the parent complex can be unambiguously determined [18–41]. This is important because, in general, there may be a range of cluster sizes present in the supersonic expansion. The ability to mass identify and uniquely select the parent is especially advantageous when there is limited spectral structure in the photodissociation absorption spectrum, as will often be the case in systems which are rapidly quenched.

The combination of tandem time-of-flight mass spectrometry with laser vaporization, hot filament or electrospray molecular beam sources has made it possible to investigate isolated weakly bound metal ion–molecule complexes in the gas phase [21–41]. This review will focus on the spectroscopy and chemical dynamics of weakly bound alkaline earth metal ion–H_2 or hydrocarbon bimolecular complexes using mass-resolved photodissociation spectroscopy techniques [33–41]. The activation of H–H, C–H and C–C bonds by metal atoms and atomic ions are among the most vital processes in chemistry, and the photodissociation spectroscopy of isolated clusters can give unique and detailed insight into the essential dynamics of these interactions [42].

Singly charged alkaline-earth-metal-ion-based complexes are ideally suited to photodissociation spectroscopy experiments because they support strong metal-centred transitions that are easily accessed in the visible and near ultraviolet (UV). Because of their open-shell 'radical' structure, non-adiabatic interactions will be especially important and chemical quenching pathways will often be open. For the lighter metal ions, detailed theoretical modelling should be feasible, making these systems ideal for fundamental studies of non-adiabatic molecular dynamics.

It is also worth noting that, while our discussion is focused on metal ion–hydrocarbon chemistry, the chemical dynamics observed in these systems are essentially similar to those of the analogous *neutral* metal hydrocarbon reactions. While it is beyond the scope of this review to do full justice to the extensive studies of neutral metal atom–hydrocarbon chemistry, we shall note instances where the dynamical models which have been developed to explain the chemistry of neutral metal atoms can also be applied to metal *ion* interactions. Despite the differences in energetics and long-range forces, the short-range chemical interactions are often remarkably similar. For example, in several of the systems discussed, photochemistry initiated on an excited-state surface followed by a non-adiabatic transition through a conical intersection or avoided crossing region to the ground state surface. The dynamical mechanism for this non-adiabatic coupling often involves a bond-stretch process originally proposed to explain the efficient quenching in excited neutral metal atom–molecule collisions [43, 44]. The experiments that we describe here represent the 'half-collision' analogue of these gas-phase quenching experiments. Photodissociation spectroscopy of a weakly bound metal ion–molecule complex can thus serve as a model system for probing fundamental issues of bimolecular dynamics, and particularly the crucial role of non-adiabatic interactions in controlling the chemical branching.

Bound metal ion–hydrocarbon complexes or clusters, isolated in the gas phase, can

also serve as useful microscopic model systems for investigating bulk interactions, as are important in solution phase inorganic and organometallic chemistry [45], chemical synthesis in bulk zeolite matrices [46] or in heterogeneous catalysis on bulk metal surfaces. Often ion–molecule reactions in the bulk proceed through a weakly bound ion–molecule cluster. Unfortunately, it is difficult to probe the structure and bonding of the complex or to determine unambiguously the important dynamical pathways within the bulk environment.

Bulk effects cause a shift and broadening in the electronic spectra which can lead to an overlapping of the observed absorption bands, complicating the spectral assignments [45]. Line broadening can obscure resonances making it very difficult to get detailed structural information about the ion–molecule complex from the electronic absorption spectra in bulk phase. Interactions with the bulk can modify reaction barriers or induce non-adiabatic coupling between electronic surfaces, opening new channels for reaction and energy disposal.

Photochemical processes in the bulk often involve several steps, some of which occur on ultrafast time scales [45]. Generally, the chemical products can be identified only after escape from the bulk cage surrounding the chromophore and cage effects can then have a profound influence on the observed quantum yields and photochemical branching ratios. This can make it hard to discern the primary intramolecular dynamics. For example, in many systems, direct charge transfer or energy transfer compete with indirect processes that follow relaxation through intersystem crossing to a low-lying long-lived state. It is difficult to unravel the role of the solvent in determining the observed rates, both through caging the nascent photoproducts and through solvent induced nonadiabatic interactions. Since the spectral assignment of a band (e.g. metal centred, ligand centred or charge transfer) often relies on the observed photoproducts, these caging effects can also lead to errors in the spectral assignment in regions where the bands overlap.

Experimental methods which can identify the primary chemical processes and which can distinguish the bulk-induced or bulk-modified processes are of great interest. The photodissociation spectroscopy of isolated, weakly bound ion–molecule complexes has emerged as a powerful tool for studying the basic ion–molecule interactions that are important in bulk phase chemistry. Mass-selected photodissociation spectroscopy of isolated metal ion–hydrocarbon complexes can give clear and accurate information about the structure of the ion–molecule complex as well as the nature and strength of the metal ion–ligand bonding. In the absence of the bulk environment, vibrational and, in favourable cases, rotational state resolution is possible and yields specific structural information on the complex geometry as well as bond strengths for both ground and electronic excited states of the complex.

The study of isolated complexes also allows a direct measure of the quantum yield for competing reactive and non-reactive quenching processes in the primary photochemical step (e.g. charge transfer on internal conversion), and in the absence of bulk caging interactions. Finally, studies of partially solvated clusters can give direct information about the effect of solvation on the structure, spectroscopy and non-adiabatic interactions of the chromophore, and the effect of the solvent cage on the subsequent chemical dynamics. These ideas have driven much of the research in this field [18–41].

2. Experimental methods

Photodissociation spectroscopy is the primary experimental tool for the investigation of the spectroscopy and photochemistry of weakly bound metal ion–molecule

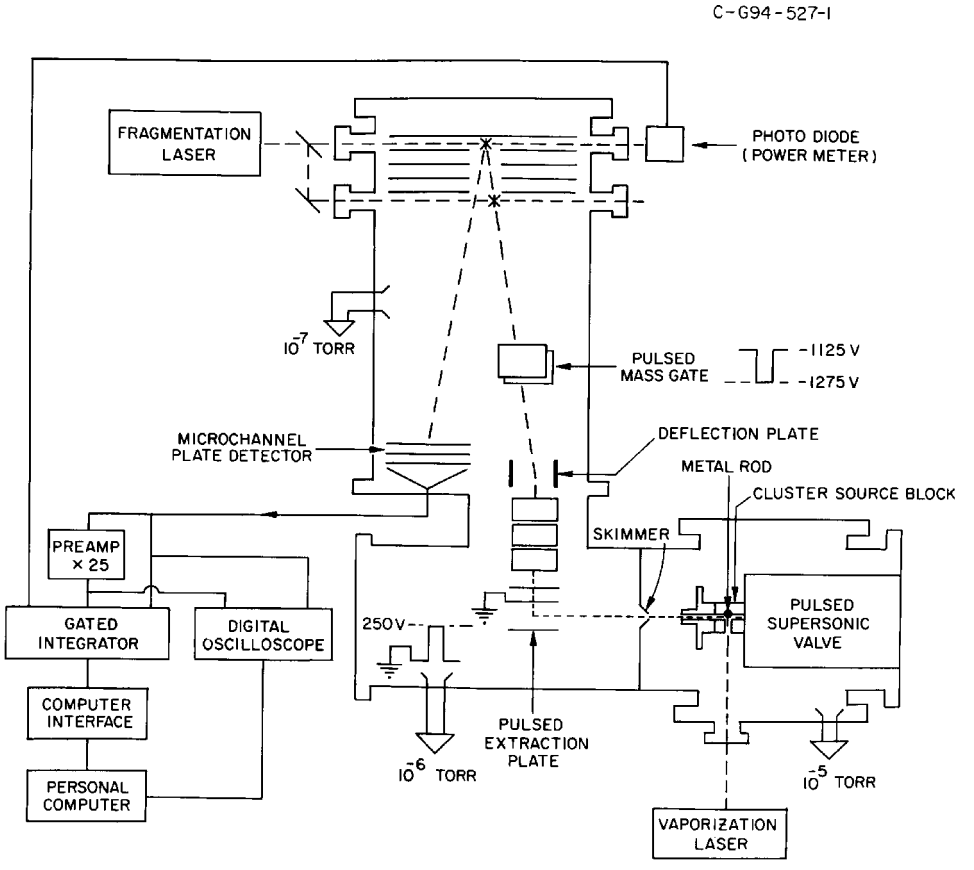

Figure 1. Block diagram of the angular RTOFMS.

clusters [47, 48]. The experimental apparatus for our work is typical [34], consisting of a Smalley-type laser vaporization cluster source [49], coupled to an angular reflectron time-of-flight mass spectrometer (RTOFMS) (figure 1). Mass-selected cluster ions are probed spectroscopically with a tunable UV–visible pulsed-laser system in the region of the reflectron. The fragment ions are mass analysed in the second leg of the RTOFMS and detected with a multichannel plate detector in a standard tandem time-of-flight arrangement. Signals are collected with a gated integrator, digital storage scope or multichannel scalar, depending on the signal level. In favourable cases, the centre-of-mass kinetic energy release in the dissociation is substantial and may allow a measure of the fragment ion translational energy distribution function by a direct inversion of the observed fragment flight-time profile [36]. This energy partitioning can give information about the lifetime of the excited intermediate and the dissociation mechanism.

Metal ions are generated by laser ablation of a solid metal rod using the second harmonic of a pulsed Nd–yttrium aluminium garnet (Nd:YAG) laser. Our efforts utilize a metal rod mounted in a source block affixed to the face of a supersonic pulsed gas valve (PGV). The ablation pulse is timed to overlap the gas pulse from the PGV and is adjusted to optimize formation of the desired cluster. The PGV is typically operated at a backing pressure of about 40 psi, seeded with a 1–10% mix of sample gas

in a He carrier gas. In many cases we have found empirically that the addition of trace amounts of impurity gas (e.g. H_2O or CO_2) aid in the formation of weakly bound clusters. The additional impurities generally cause no mass confusion in this tandem time-of-flight arrangement. The sample rod is connected to a drive mechanism allowing for simultaneous rotation and translation of the rod to keep the metal sample surface fresh. Several variations on the source geometry have been successfully used including a longitudinal geometry [37] as well as the more traditional transverse arrangement [34], each with a gas flow channel designed to enhance complex formation. The source block in our apparatus is in thermal contact with a liquid-N_2 reservoir so that the gas flow channel can be conductively cooled to temperatures as low as about 100 K. However, recently we and others have found that cold bimolecular complexes can be readily formed by laser ablation of the metal rod positioned directly in the free jet expansion from the PGV nozzle (essentially eliminating the gas flow channel) [28, 41]. The ablation laser pulse intensity is kept low to minimize overheating of the laser produced plasma and to optimize the formation of weakly bound bimolecular complexes with low internal temperatures. Too large a laser fluence results in warmer clusters, greater fragmentation and more 'pre-reaction' in the source region.

Weakly bound clusters are formed in the supersonic expansion of the metal vapour plasma with a seeded carrier gas flow. The gas expansion passes through a conical skimmer into the differentially pumped extraction chamber. The nozzle-to-skimmer distance is much less than the distance to the Mach disc. Cluster ions are pulse extracted at right angles and accelerated into the third differentially pumped chamber, the flight tube of the RTOFMS. The typical beam energy is 1.4 keV. The ion packets are transversely focused with a three-element Einzel lens and pass through a pulsed mass gate for preliminary mass selection. The RTOFMS is a modified version of a commercial instrument; the flight tube and ion optics are shielded and isolated from ground so that they can be floated at the acceleration voltage. The extraction and acceleration voltages are adjusted to achieve a Wiley–McLaren [50] focus at the laser probe spot.

A Nd:YAG pumped tunable pulsed dye laser, with nonlinear frequency mixing capabilities is time delayed to excite the 'target' parent ion. Our RTOFMS is designed so that photodissociation can be carried out either at the turning point inside the reflectron, or 'on the fly', that is at the Wiley–Mclaren focus in the flight tube just before the entrance to the reflectron. Each approach has advantages and disadvantages. When dissociating at the turning point in the reflectron, fluctuations due to timing jitter can be minimized since the residence time near the turning point is long. In addition, accurate branching ratio measurements are more easily made because the unreacted parent ion and all the daughter ions may be detected simultaneously. (This assumes that mass discrimination effects are negligible, which is usually a good approximation in our apparatus for the small clusters of interest here [37, 47].)

Alternatively, dissociation can be carried out 'on the fly'. Because the dimensions of the ion packet at the focus are small relative to the laser spot size and pulse length, this arrangement affords better mass resolution for the photodissociation probe step. In addition, it is easier to carry out quantitative measurements of the photofragment kinetic energy release in this arrangement as discussed below. In most cases we have used this second arrangement and carried out the photolysis at a Wiley–McLaren focal spot about 1 cm before the entrance to the reflection. The reflectron voltages are then adjusted to give a second focal point at the off-axis microchannel plate (MCP)

detector [51]. The disadvantage is that, for the same reflectron focusing conditions, the parent and the daughter ions will have different trajectories through the reflectron and mass discrimination effects become significant. Because the reflectron focusing conditions are mass dependent, they must be readjusted to ensure proper focusing for each daughter ion, making accurate branching ratio measurements more cumbersome and tedious.

In either arrangement, parent and daughter fragment ions are reaccelerated in the reflectron and focused to an off-axis 40 mm MCP detector. A digital oscilloscope is used to monitor the mass spectrum and is interfaced to a laboratory personal computer for further data analysis. When signals are large, a series of gated integrators can be used to measure the integrated signal in the parent and in each daughter ion packet. For small signals, a multichannel scaler can be used for single-ion counting.

The mass-resolved product action spectra are determined by measuring the integrated daughter ion signal as a function of photolysis laser wavelength, normalized by the parent ion signal and probe laser intensity. The signal-to-noise ratio is limited primarily by short-term fluctuations and long-term drift in the molecular beam intensity from our laser vaporization source, and by timing jitter between the laser pulse and the ion packet at the probe spot.

Information about the energy partitioning can allow far more detailed insight into the dissociation dynamics. For measurement of the fragment translational energy release distribution function and vector anisotropy, we have adapted conventional approaches to our experimental requirements [36, 52–56]. Essentially, the observed daughter ion flight-time profile is related to a one-dimensional projection of the speed distribution function, convoluted with an anisotropy function and an instrument profile. For measurements taken at the magic angle polarization, the photofragment anisotropy effect vanishes and the speed distribution function can be extracted by deconvoluting the instrument function. By varying the laser polarization, the photofragment anisotropy parameter can also be determined [17, 36].

For measurement of the mass-resolved product action spectra and branching ratios, the reflectron voltages are normally chosen to refocus each daughter ion packet at the off-axis MCP detector [51]. This optimizes the mass resolution and signal collection efficiency. Under these conditions the reflectron compensates for any kinetic energy release in the fragmentation, making the observed flight-time profile independent (to first order) of the fragment centre-of-mass velocity distribution. However, we may purposely choose to operate the reflectron in a slightly defocused mode. The observed broadening in the flight time profile can then be related to the velocity release in the dissociation process through the known time-of-flight equations for our instrument. The 'best' defocused conditions must be determined empirically. Focal points too near the detector will not give a good temporal spread, while focal points too far from the detector will lead to a decrease in signal collection efficiency or to an overlapping of adjacent mass peaks because of the degraded mass resolution. Over the range of allowable reflectron focusing conditions, the observed flight-time profile will vary markedly, but the centre-of-mass speed distribution function is independent of the actual focusing conditions.

For any focusing conditions, the observed flight-time profile $h^{\alpha}(t)\,\mathrm{d}t$ can be related to the one-dimensional projection of the laboratory velocity distribution function $S^{\alpha}(V_z)\,\mathrm{d}V_z$, onto the flight tube z axis as [56]

$$h^{\alpha}(t)\,\mathrm{d}t = S^{\alpha}(V_z)\,\mathrm{d}V_z \tag{2.1}$$

through the known time-of-flight equation

$$t = t(V_z) \tag{2.2}$$

for the instrument. In equation (2.1), α is the angle between the laser polarization axis and the flight tube (z) axis. V_z is the z component of the daughter ion velocity in the laboratory frame, given by $V_z = V_{pz} + v_z$, where V_{pz} is the z projection of the parent velocity (which defines the velocity of the centre of mass), and v_z is the z projection of the daughter ion velocity relative to the centre of mass (due to kinetic energy release in the dissociation process). The time-of-flight equation (2.2) explicitly gives the flight-time from the photolysis region to the MCP detector for any ion as a function of the laboratory velocity projected onto the flight path axis. Equation (2.2) depends on the geometry and physical dimensions of the instrument, and on the bias voltages (and hence focusing conditions) of the reflectron. Thus, with equation (2.2), the observed flight-time profile can be inverted to give.

$$S^{\alpha}(V_z) = h^{\alpha}(t)\frac{\mathrm{d}t}{\mathrm{d}V_z}. \tag{2.3}$$

The 'observed' velocity function $S^{\alpha}(V_z)$ is given by a convolution of the z projection of the distribution function of parent ion velocities $R(V_{pz})$ with the z projection of the centre-of-mass velocity distribution function for the fragments $f^{\alpha}(v_z) = f^{\alpha}(V_z - V_{pz})$, that is

$$S_z^{\alpha}(V_z) = \int_{-\infty}^{\infty} \mathrm{d}V_{pz}\, R(V_{pz}) f^{\alpha}(V_z - V_{pz}). \tag{2.4}$$

$R(V_{pz})$ gives the distribution of parent ion velocities projected onto the flight path axis; it is centred about the beam velocity. This distribution arises primarily from the finite spatial spread of the parent ion packet in the extraction region of the time-of-flight apparatus and represents the primary limitation on our instrumental resolution. The deconvoluted projected daughter velocity distribution function $f^{\alpha}(v_z)$ depends on the speed release distribution function $g(v)$ and the velocity-dependent anisotropy parameter $\beta(v)$ and is given for the dissociation process by [56]

$$f^{\alpha}(v_z) = \int_{v(\mathrm{min})}^{v(\mathrm{max})} \mathrm{d}v' \frac{g(v')}{2v'}\left[1 + \beta(v')P_2(\cos\alpha)P_2\left(\frac{v_z}{v'}\right)\right], \tag{2.5}$$

where $v(\mathrm{min}) = |v_z|$ and $v(\mathrm{max}) = (v_d^2 + v_z^2)^{1/2}$, with v_d the discrimination velocity [56]. The discrimination velocity v_d is roughly equal to the detector radius divided by the flight time. For our apparatus, we estimate the discrimination velocity to be about 1000 m s^{-1}.

For simplicity we can make two approximations to (2.5). First, we assume that the velocity-dependent anisotropy parameter $\beta(v)$ can be replaced by a velocity-independent averaged value β. While not strictly correct, this assumption is common and greatly simplifies the analysis. In principle, the full velocity-dependent $\beta(v)$ parameter can be extracted from a series of measurements of the daughter ion flight-time profile at different polarization angles α. In practice this is often difficult owing to the limited velocity resolution and statistical noise inherent in the experimental measurements. Secondly, we assume (as a first approximation) that the discrimination velocity v_d is large so that the upper integration limit in equation (2.5) can be replaced by infinity. This amounts to assuming that our detector is large enough to collect all the daughter fragments. While this is also not rigorously correct, it turns out to be a

fairly good approximation and allows us to extract a first approximation to the distribution function $g(v)$, which can then be improved by iteration. With these assumptions, equation (2.5) becomes

$$f^{\alpha}(v_z) = \int_{|v_z|}^{\infty} \mathrm{d}v' \frac{g(v')}{2v'} \left[1 + \beta P_2(\cos\alpha) P_2\left(\frac{v_z}{v'}\right) \right]. \tag{2.6}$$

For flight-time profile measurements taken at the magic angle $\alpha = 54.7^{\circ}$, $P_2(\cos\alpha) = 0$ and equation (2.6) reduces to

$$f^{\mathrm{ma}}(v_z) = \int_{|v_z|}^{\infty} \mathrm{d}v' \frac{g(v')}{2v'} \tag{2.7}$$

and hence $g(v)$ may be obtained by numerical differentiation:

$$g(v) = 2v \left| \frac{\mathrm{d}f^{\mathrm{ma}}(v)}{\mathrm{d}v} \right|. \tag{2.8}$$

Given $g(v)$, β can be determined by fitting equation (2.6) for measurements taken at other polarization angles, typically $\alpha = 0$ or 90°.

The main sources of error in this procedure are in the deconvolution of the instrument response function. Generally the instrument function is not well known and the deconvolution procedure invariably introduces some broadening of the distributions. Nevertheless, the results can give useful and reliable information about the photofragment translational energy release and anisotropy, particularly when the energy release is large. In that case the effective flight time broadening in the profile can be substantial and the uncertainty in the precise form of the instrument response function is not a significant limitation.

The analysis is discussed in detail and applied to an analysis of the photofragment energy release and anisotropy in photodissociation of $Mg_2CH_4^+$ in [32]. We have used similar methods to obtain information about the photofragment kinetic energy release in several metal ion–hydorcarbon bimolecular complexes [36, 38, 41].

3. Photodissociation spectroscopy of alkaline-earth metal ion–molecule complexes

3.1. *Photoactivation of H–H bonds*

3.1.1. MgD_2^+

The study of the spectroscopy and chemical dynamics of MgH_2^+ represents one of the simplest and most fundamentally important applications of these experimental methods. MgH_2^+ can serve as a prototype system for the investigation of reactive quenching dynamics through a conical intersection, a process of theoretical interest in molecular dynamics and considerable importance in organic photochemistry. The MgH_2^+ complex is only weakly bound, but stable complexes of the isotopic derivative, MgD_2^+, have been formed in a liquid-N_2-cooled longitudinal laser vaporization source and studied by mass-resolved photofragmentation spectroscopy in our laboratory [37]. (MgD_2^+ was chosen over MgH_2^+ for experimental convenience in assigning and resolving the photofragment mass spectrum as discussed in [37].)

Electronic structure calculations by Bauschlicher [57] have shown MgH_2^+ to be weakly bound in a $1\,^2A_1$ ground state in C_{2v} geometry with $D_e = 0.095$ eV and a $Mg^+–H_2$ bond midpoint equilibrium separation $R_{Mg-X} = 2.72$ Å [57]. The ground-state equilibrium H_2 bond length is $r_{H-H} = 0.745$ Å, close to the relaxed value of 0.741 Å in isolated H_2. The ground-state binding is enhanced somewhat by the mixing of some

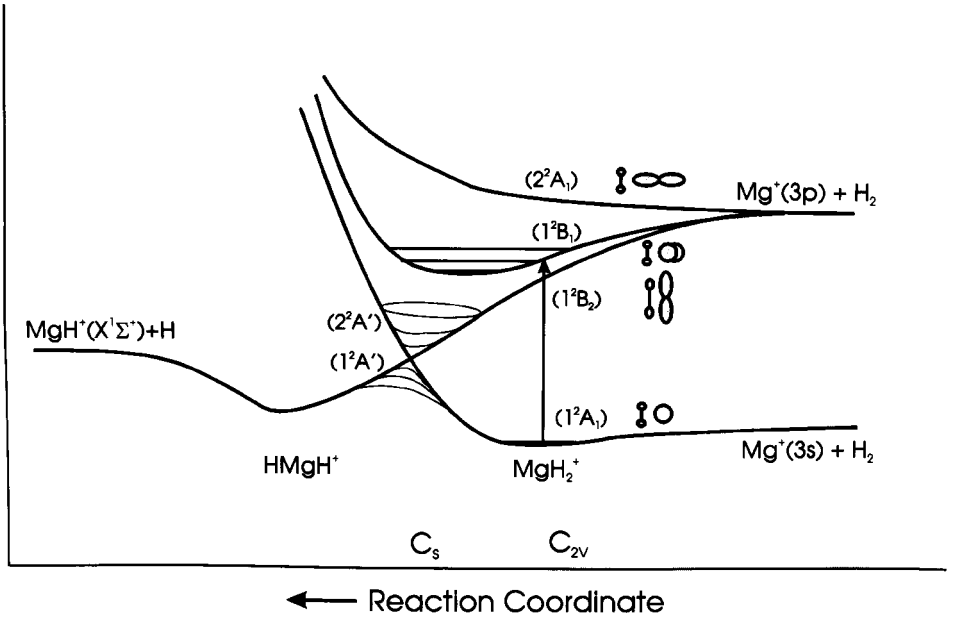

Figure 2. Schematic reaction path for the dissociation of MgD_2^+.

3pσ character into the '3s' orbital which allows the ground-state orbital to polarize away from the H_2, reducing the Mg–H_2 repulsion. Bauschlischer [57] has also carried out *ab-initio* calculations for the excited 1 $^2B_2$, 1 $^2B_1$, and 2 $^2A_1$ molecular states of the complex, correlating with the Mg^+ (3s–3p) atomic resonance transition at 280 nm; the states of distinct molecular symmetry corresponding to the three symmetric alignments of the Mg*(3p) orbital with respect to the H–H bond. These are schematically represented in figure 2. The 2 $^2A_1$ state is essentially repulsive in the Mg^+–H_2 coordinate. This is expected since, in this symmetry, the Mg^+ '3s3p' hybridized orbital is directed towards the ligand, leading to a long-range electron repulsion. On the other hand, in the states of $^2B_1$ and $^2B_2$ symmetry the Mg^+ 'p' orbital is aligned away from the H_2 ligand, either out of the Mg–H–H plane ($^2B_1$), or in the Mg–H–H plane and parallel to the H–H bond axis ($^2B_2$). These symmetries reduce the orbital overlap which lessens the Mg–H_2 repulsion. In addition the geometry exposes the metal ion core enhancing the electrostatic attraction. The result is that both the excited $^2B_1$ and the excited $^2B_2$ states are attractive at long range.

The 1 $^2B_1$ state is moderately bound in the excited state by $D_e = 0.80$ eV, and with a potential minimum at $R_{Mg-X} = 1.94$ Å. Again the equilibrium H_2 bond length ($r_{H-H} = 0.765$ Å) is close to relaxed value in isolated H_2. In contrast, the 1 $^2B_2$ state is much more strongly bound ($D_e = 1.96$ eV) and shows appreciable insertion character with the metal ion inserting into the H–H bond to form a bent H–Mg^+–H species with $R_{Mg-X} = 1.36$ Å, a bond angle of 81.7° and severely stretched H–H bond ($r_{H-H} = 2.35$ Å). In this insertion geometry, the Mg^+–H bond length (1.80 Å) is already fairly close to its relaxed value in the isolated MgH^+ diatomic (1.65 Å), suggesting that the H–H bond has 'already broken', and the Mg^+–H bond 'already formed' in the excited state. This insertion character in the 1 $^2B_2$ state is fully consistent with expectations based on a bond-stretch model proposed by Hertel [43] to explain the efficient E–V quenching of Na*(3p) by H_2, and by Breckenridge [44] to explain the efficient reactive quenching in the analogous neutral system Mg*(3p)+ H_2.

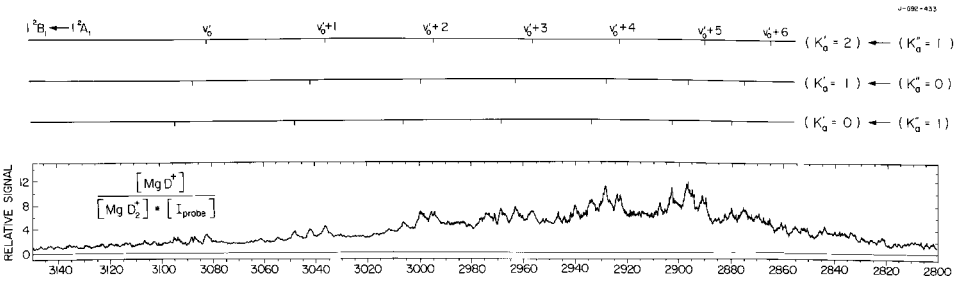

Figure 3. Action spectrum for photofragmentation of MgD_2^+ to MgD_2. No non-reactive photoproduct was observed. The wavelength is given in angströms. (From [37].)

Predicted spectroscopic parameters for MgD_2^+ can be obtained from the *ab initio* results for MgH_2^+ by using mass-reduced values as appropriate and are compared with the spectroscopic results below.

We studied the photodissociation spectroscopy of MgD_2^+ in the spectral region of the $2\,^2A_1$, $1\,^2B_2$ and $1\,^2B_1 \leftarrow 1\,^2A_1$ molecular bands correlating with the $Mg^+(3s–3p)$ resonance transition [33]. The possible photofragmentation processes can be described as

$$MgD_2^+ + h\nu \rightarrow (MgD_2^+)^* \rightarrow Mg^+{}^*(3p) + D_2 \qquad \text{(direct dissociation)}, \tag{3.1}$$

$$\rightarrow Mg^+(3s) + D_2^\dagger(v) \qquad \text{(pre-dissociation)}, \tag{3.2}$$

$$\rightarrow MgD^+ + D \qquad \text{(reaction)}. \tag{3.3}$$

To the blue of the $Mg^+(3s–3p)$ resonance line ($\lambda < 280$ nm), excitation of the repulsive $2\,^2A_1$ state leads exclusively to direct $Mg^+–D_2$ bond breaking and dissociation to $Mg^+{}^*(3p) + D_2$ as expected (channel (3.1)).

More interesting is the spectral region to the red of the $Mg^+(3s–3p)$ resonance line, where the direct dissociation channel is not energetically accessible. In this spectral range (280–314 nm), *only* the reactive dissociation channel (3.3) was observed; pre-dissociation (3.2), corresponding to the 'half-collision' analogue of E–V quenching, was not detected. The MgD^+ reactive action spectrum, reproduced in figure 3, consists of a series of discrete vibrational transitions with rotational substructure, superimposed on a broad structureless continuum.

The observed spectrum has been assigned to the perpendicular transitions $1\,^2B_{1,2} \leftarrow 1\,^2A_1$ in C_{2v} geometry [37]. Specifically the underlying continuum was assigned to the $1\,^2B_2 \leftarrow 1^2A_1$ transition. Reaction on this surface is likely to be direct and rapid through a bond-stretch mechanism. The alignment of the Mg^+ 'p' orbital in the $1\,^2B_2$ state of MgH_2^+ affords the opportunity for good molecular orbital overlap with the σ^* antibonding orbital of H_2. This allows for efficient transfer of electron density from the $Mg^+{}^*(3p)$ orbital into the σ^* antibonding orbital of H_2, weakening and stretching the H–H bond. Because of the relatively large size of the $Mg^+{}^*(3p)$ orbital, the orbital overlap is enhance by the H–H bond stretch. In addition, donation of electron density from the H_2 σ bonding orbital into the empty s orbital of Mg^+ further enhances the interaction and strengthens the $Mg^+–H$ bond. This bond-stretch mechanism predicts a strong electronic orbital alignment selectivity for reactive quenching in MgD_2^+, in complete agreement with experimental results.

In C_s symmetry, the ground state of the reactants $Mg^+(3s)+H_2$ is $^2A'$ and correlates adiabatically with the ground state ($^2A'$:$(n\sigma)^2(p\sigma)$) of the insertion complex $H-Mg^+-H$. However, there is a large activation barrier for insertion on the ground state surface. This is because the ground state ($^2A'$:$(n\sigma)^2(p\sigma)$) of the insertion complex $H-Mg^+-H$ correlates (in a molecular orbital sense) to an excited state of the reactants $Mg^{+*}+H_2$, while the ground state of the reactants $Mg^+(3s)+H_2$ correlates (in a molecular orbital sense) to an excited state $(s\sigma)^2(s\sigma^*)$ of $H-Mg^+-H$ [44]. This leads to a high avoided crossing energy barrier to insertion on the ground-state surface.

The result is that, as the Mg^+ approaches H_2 from the ground-state equilibrium distance, the ground-state ($1\,^2A_1$) surface is steeply repulsive and is expected to cross the excited ($1\,^2B_2$) surface, in a C_{2v} symmetry-allowed crossing seam. In C_{2v} geometry, and with the internal coordinates of H_2 fixed, there will be a single crossing point as a function of the Mg^+-H_2 intermolecular distance. For slightly off-axis geometries (C_s symmetry) the $1\,^2B_2$ and $1\,^2A_1$ surfaces are both $^2A'$ character and will show an avoided crossing, leading to a typical conical intersection as shown schematically in figure 2. In higher dimensionality (as the internal coordinates of H_2 vary), this conical intersection becomes a crossing seam in the potential energy hypersurfaces. The conical intersection allows a path for efficient quenching to the ground-state surface with no significant activation barrier. In an *ab-initio* calculation on the Gaussian '94 platform, we were able to identify a portion of such a crossing seam near the $^2B_2$ minimum for MgH_2^+ by geometry optimization to a curve-crossing point [58]. The seam is energetically accessible from the initial geometry on the $^2B_2$ surface (i.e. from the region of Franck–Condon excitation from the ground state equilibrium). (The crossing seam in C_{2v} symmetry is similar to that represented later in figure 10 for the $MgC_2H_4^+$ ion–molecule system described below.) These results firmly support the proposed reactive quenching pathway.

The reactive quenching mechanism postulated here, involving a non-adiabatic transition through a region of conical intersection in near-C_{2v} geometry, is virtually identical with that proposed for the efficient E–V quenching in the isoelectronic system

$$Na^*(3p)+H_2 \rightarrow Na(3s)+H_2(v) \tag{3.4}$$

(where reactive channels are not energetically accessible under normal experimental conditions) [43]. Significant theoretical effort, including both accurate *ab-initio* potential surface calculation and semiclassical and quantum dynamics calculations have led to a clear understanding of the *non-reactive* quenching dynamics through this bond-stretch process in $Na^*(3p)+H_2$ [59, 60].

More extensive experimental effort has been focused on the neutral atom chemical reactions involving both alkali and alkaline earth atoms in their 'p' states with H_2. For example the analogous neutral reactions

$$Mg^*(3p)+H_2 \rightarrow MgH(v,J)+H \tag{3.5}$$

and

$$Na^*(4p)+H_2 \rightarrow NaH(v,J)+H \tag{3.6}$$

have been studied in detail. The work includes both 'full-collision' state-to-state measurements of the product rovibrational quantum state distribution and 'half-collision' scattering state spectroscopic studies of the transient reaction complex [61–65]. This experimental work and supporting *ab-initio* calculations also provide

evidence for a reaction mechanism involving the non-adiabatic passage through a conical intersection or narrowly avoided crossing region in near C_{2v} symmetry [44, 62]. Breckenridge [44] has recently reviewed the closely related chemistry of neutral alkaline earth metal atoms in their ^{3}P and ^{1}P excited states with H_2, CH_4 and SiH_4 [44].

The reasons for the observed predominance for the reactive quenching channel (over non-reactive E–V quenching) are not obvious, although as noted above, the 'late' geometry of the insertion complex suggests that the H−H bond has 'already broken' and the Mg^+−H bond has 'already formed' in the excited state, before the non-adiabatic transition to the ground-state surface.

The presence of sharp discrete vibrational absorption bands in the reactive fragmentation channel indicates a second indirect reaction mechanism through a long-lived excited-state complex. This structure has been assigned to the $1\,^2B_1 \leftarrow 1\,^2A_1$ transition. Reaction occurs indirectly, possibly through a weak Coriolis coupling to the $1\,^2B_2$ state. The spectrum shows a vibrational progression with decreasing spacings from 489 to 314 cm^{-1}. Unfortunately, because of the large change in R_{Mg-X} on excitation to the $1\,^2B_1$ state, the excited-state origin was not Franck–Condon accessible and the absolute vibrational numbering is uncertain. Nevertheless, the observed values compare favourably with the expected value for $\omega_e = 588$ cm^{-1} (based on *ab-initio* calculations), given the observed anharmonicity ($\omega_e x_e = -14$ cm^{-1}) [57]. The discrete structure within a given vibrational band was assigned to resolved K-subband rotational transitions ($K_{a''} = 0 \rightarrow K_{a'} = 1$ and $K_{a'} = 0, 2$) in *ortho*- and *para*-MgD_2^+ respectively. A-axis rotational constants (for rotation about the C_2 symmetry axis, corresponding to the propeller motion of D_2) can be derived from a simulation of the observed K-subband rotational structure. The experimental rotational constants ($A'' = 34 \pm 4$ cm^{-1} and $A' = 32 \pm 4$ cm^{-1}) are in good agreement with predictions derived from the *ab-initio* structure calculations ($A'' = 30$ cm^{-1} and $A' \approx 29$ cm^{-1}] [57]. Additional unassigned peaks in the spectrum are consistent with vibrational hot bands. Results of the rotational spectrum simulation for one of the members of the vibrational series are shown in figure 4 [37(b)]. The resolved rotational peaks are broad; the spectral simulation gives a homogeneous linewidth of about 25 cm^{-1}, consistent with a pre-dissociation lifetime of about 0.2 ps.

Breckenridge and co-workers [66] have also seen very similar spectroscopic evidence for an electronic orbital alignment dependence on the quenching rate in the photodissociation of neutral CdH_2 van der Waals complexes. The action spectrum for excitation to the red of the Cd($5p\,^1P$–$5s\,^1S$) resonance transition in CdH_2 consists of a lifetime-broadened continuum with overlapping discrete vibrational resonances. As in the spectrum for MgD_2^+ discussed above, the continuum band was assigned to excitation of the molecular state $CdH_2(5p\pi\,(^1B_2))$, resulting in rapid reaction or pre-dissociation. The discrete spectrum was assigned to excitation of the $CdH_2(5p\pi\,(^1B_1))$ molecular state, which was quenched only slowly through a spin–orbit curve crossing.

The dissociation model proposed here must still be considered qualitative and hence incomplete. While it is fully consistent with the experimental observations and with the available electronic structure calculations, more extensive *ab-initio* calculations of the region of the expected conical intersection are required for quantitative modelling. For example, it is important to know whether additional regions of non-adiabatic coupling might be significant. Molecular dynamics calculations based on surface hopping methods or even full quantum dynamics methods should be possible and may help to explain further the dramatic preference for the reactive quenching channel in this prototype system.

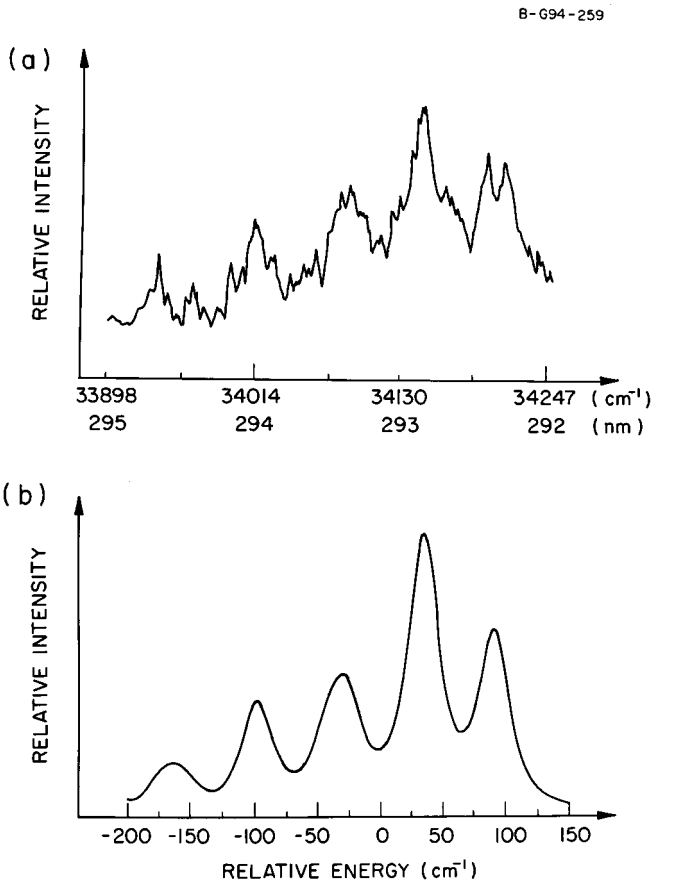

Figure 4. Simulation of the *K*-subband rotational spectrum for the $v_0 + 4$ vibronic resonance in figure 3. The simulation assumes a rotational temperature of 30 K, a vibrational temperature of 200 K, and a homogeneous linewidth of 25 cm^{-1}. (From [37(b)].)

3.2. *Photoactivation of C–H bonds*

3.2.1. $MgCH_4^+$

Metal activation of C–H bonds is one of the most significant processes in chemistry. It has long been recognized that the reactions of metal atoms with CH_4 are, in most cases, more inefficient than the corresponding reaction with H_2, despite the fact that the C–H and the H–H bonds are comparable in strength [44, 67]. There are often substantial activation barriers for the chemical quenching of the low-lying excited states metal atoms by alkane hydrocarbons [44]. These activation barriers may result from steric hindrance effects due to repulsion between the metal atom orbitals and other nearby C–H and C–C localized bonding orbitals. This can limit the close approach of the metal atom to the C–H bond under attack, restricting the overlap between the metal atom valence orbitals and the localized C–H(σ^*) antibonding orbital. The directed nature of the C–H bond may also play a role in constraining the effective orbital overlap [68, 69].

One of the simplest metal ion–hydrocarbon complexes, namely $MgCH_4^+$, also represents an important prototype bimolecular model system for half-collision studies of metal activation of C–H bonds in alkanes. The photodissociation spectroscopy of $MgCH_4^+$ has also been studied in our laboratory [38].

$MgCH_4^+$ molecular absorption bands were observed to the red of the $Mg^+(3\,^2P_J \leftarrow 3\,^2S_{1/2})$ atomic ion resonance lines. The photofragmentation action spectrum consists of a broad structureless continuum ranging from 310 to 342 nm, peaking near 325 nm. In this spectral region, both the non-reactive (Mg^+), and two reactive fragmentation products (MgH^+ and $MgCH_3^+$) were observed, all with similar action spectra.

These energetically accessible channels can be schematically described as

$$MgCH_4^+ + h\nu \rightarrow (MgCH_4^+)^* \rightarrow Mg^+{}^*(3p) + CH_4 \quad \text{(direct dissociation)}, \tag{3.7}$$

$$\rightarrow Mg^+ + CH_4 \quad \text{(pre-dissociation)}, \tag{3.8}$$

$$\rightarrow MgH^+ + CH_3 \quad \text{(reaction to hydride)}, \tag{3.9}$$

$$\rightarrow MgCH_3^+ + H \quad \text{(reaction to methyl)}. \tag{3.10}$$

As in MgH_2^+ the direct dissociation channel (3.7) is only energetically open when the laser is tuned well to the blue of the $Mg^+(3s–3p)$ resonance transition. Our interest lies in the quenching channels (3.8)–(3.10) which could be accessed by excitation of the $Mg^+(3p\pi)$ states to the red of the $Mg^+(3s–3p)$ resonance line.

Bauschlicher and Sodupe [70] have carried out theoretical *ab-initio* calculations of the $MgCH_4^+$ complex. They found that the complex is weakly bound by electrostatic interactions in C_{3v} geometry with η_3 facial coordination, and with a ground state ($1\,^2A_1$) binding energy $D_0'' = 0.31$ eV. Under these conditions there is little distortion of the CH_4 ligand. Bauschlicher and Sodupe also predicted T_e values for the molecular states correlating with the $Mg^+{}^*(3p\,^2P)$ first excited level. In these excited states there is a significant geometry change to C_{2v} with η_2 coordination; as in MgH_2^+, the $1\,^2B_1$ and $1\,^2B_2$ surfaces are attractive while the $2\,^2A_1$ surface is repulsive. Based on these calculations the observed molecular absorption continuum band was assigned to the transition ($1\,^2E \leftarrow 1\,^2A_1$) in C_{3v} geometry, followed by a geometrical relaxation towards the attractive surfaces of $^2B_1$ and $^2B_2$ character in C_{2v} geometry. Because of the large geometry change on excitation, the transition to these states is expected to be broad, with a high density of final states. Homogenous broadening of the excited-state energy levels due to rapid pre-dissociation or reaction is also expected to be significant. The observation of a broad structureless absorption continuum was consistent with these expectations.

Both non-reactive (channel (3.8)) and reactive fragmentation products (channels (3.9) and (3.10)) were observed, all with similar action spectra. The product branching was found to be independent of wavelength, but non-statistical:

$$Mg^+ : MgCH_3^+ : MgH^+ \approx 60 : 33 : 7.$$

This observation suggested that the final state branching is determined primarily by exit channel dynamical effects, following passage through an early dissociative transition state. Because photoexcitation is significantly to the red of the Mg^+ resonance line, direct dissociation on the excited-state surface was not energetically allowed; dissociation in each channel (3.8)–(3.10) must involve a non-adiabatic transition to the ground-state surface.

On the basis of the observed branching to the $MgCH_3^+$ methyl product, it is clear that a significant fraction of the reactive trajectories must sample 'insertion-like' geometries. As noted above there are often substantial activation barriers to C–H

Table 1. Total translational energy release in the non-reactive photodissociation of $MgCH_4^+$ and $MgCD_4^+$. (From [37].)

Photolysis wavelength (nm)	Energy release (cm^{-1}) for the following parent clusters	
	$MgCH_4^+$	$MgCD_4^+$
332.5	370 ± 150	540 ± 180
315.9	520 ± 180	830 ± 200

bond insertion in metal atom–alkane reactions. In the photolysis of $MgCH_4^+$, however, reactive quenching by C–H bond activation is a major decay channel, with a quantum yield of about 40%. Furthermore, this value is roughly independent of photolysis wavelength, indicating that the region of Franck–Condon excitation on the excited-state surface must lie well above any local barrier on the potential energy surfaces. Efficient chemical quenching has also been found in the analogous neutral Mg*(3p ^{1}P)+ CH_4 reaction [71, 72].

It should be noted that the Mg^+–H and Mg–CH_3^+ bond strengths are expected to be similar, so that the preference for the reactive methyl product over the hydride product ($MgCH_3^+$-to-MgH^+ ratio, about 5) cannot be easily explained by the energetics alone [38]. This suggests that exit channel dynamical effects play a significant role in determining the product branching. Further experimental evidence that the dissociation is direct and that exit channel dynamics play a crucial role comes from measurement of the product kinetic energy release [38].

Analysis of the broadening in the photofragment flight time profile, as discussed in section 2 above, showed the average translational energy release in the non-reactive Mg^+ channel to be very low. Because of this the flight-time broadening was small and there was significant uncertainty in the deconvolution procedure (2.4). Nevertheless the measurement placed an upper limit on the photofragment kinetic energy and showed that the total translational energy release was anomalously low relative to statistical model predictions. Additional experiments showed that the observed kinetic energy release in the non-reactive channel was a strong function of photon energy, and significantly larger for the dissociation of $MgCD_4^+$ (table 1). These results demonstrate that the dissociation is non-statistical, and that dynamical effects play a central role in determining the energy partitioning.

These experimental observations suggested a dynamical mechanism for the dissociation. Following excitation of the ^{2}E surface in C_{3v} (η_3) geometry, the complex relaxes to the $^2B_1$ and $^2B_2$ states in C_{2v} (η_2) geometry. The complex then passes through a distorted triangular H–Mg^+–CH_3 dissociative transition state, corresponding to a region of avoided potential surface crossing which opens a path for a non-adiabatic transition to the ground-electronic-state surface.

In an effort to determine the geometry of the dissociative transition state, a series of preliminary CIS (configuration interaction with single excitation) calculations were carried out for the lowest excited A′ and A″ potential energy surfaces of the H–Mg^+–CH_3 triangular complex in C_s symmetry [38]. The results suggested a region of narrowly avoided crossing between the lowest two surfaces of A′ character. The calculation was not sufficiently accurate for a reliable quantitative evaluation of the avoided crossing region; however, the qualitative nature of the potential energy surfaces is reasonable.

The $MgCH_4^+$ geometry in the avoided crossing region, which is presumed to correspond to the dissociative transition state, shows that the C–H bond under attack is severely stretched but not broken, with $R_{C-H} = 1.71$ Å (which can be compared with the unstretched C–H bond length in methane of 1.09 Å). Furthermore, the *ab-initio* results suggest that the Mg^+–H bond length ($R_{Mg-H} = 1.66$ Å) and the Mg^+–C bond length ($R_{Mg-C} = 2.01$ Å) in the transition-state geometry are both close to their isolated equilibrium values in MgH^+ ($R_{Mg-H} = 1.65$ Å) and $MgCH_3^+$ ($R_{Mg-C} = 2.08$ Å) respectively [38]. This geometry is consistent with the approach to an insertion-type quenching pathway, but which is hindered by repulsion from the orbitals associated with the remaining methyl group. Indeed, the complex has distorted from the ground-state equilibrium, with the remaining C–H bonds of the methyl group pushed away, presumably to minimize the orbital repulsion between the metal ion 'p' orbital and the σ bonds on the methyl group, easing the steric hindrance. The 'insertion' may be facilitated by orbital overlap between the in-plane 'p' orbital on the Mg^+ and the lowest σ* antibonding orbital centred on the C–H bond in A′ symmetry, allowing for transfer of electron density into the antibonding orbital. This results in a weakening and stretching of the C–H bond in a bond-stretch picture analogous to that described above for the MgD_2^+ case.

Dissociation follows the non-adiabatic transition to the ground state. Reaction on the ground-state surface might involve full insertion into a long-lived nearly linear $H–Mg^+–CH_3$ intermediate; however, consistent with the non-statistical branching, it seems more likely that dissociation follows impulsively from the bent dissociative intermediate, with the product branching and energy partitioning determined by dynamical effects on an anisotropic ground-state surface, roughly independent of excitation wavelength.

A simple kinematic model was also developed which could explain the kinetic energy release data in the non-reactive dissociation channel, including both the observed photon energy dependence and the isotope dependence [38]. This phenomenological model was based on energy and momentum conservation and assumed a direct and anisotropic dissociation from a distorted $H–Mg^+–CH_3$ triangular intermediate, leaving the nascent CH_4 photofragment highly excited, both vibrationally and rotationally.

The proposed reaction pathway involving a C–H σ bond-stretch mechanism is consistent with experimental observations and the limited available *ab-initio* data [34]. It is analogous to that described above for the reactive quenching in MgD_2^+. This mechanism is also essentially similar to that proposed to explain the product state branching and the observed electronic alignment preference in the analogous neutral atom reaction [71–74]

$$Mg^*(3p\ ^1P) + CH_4 \rightarrow MgH + CH_3. \tag{3.11}$$

Unfortunately, the *ab-initio* calculations are clearly insufficient and not accurate enough to support a definitive interpretation [38]. For example, it is not certain whether the coupling region is a true conical intersection or simply a region of narrowly avoided crossing. It is not even certain whether the region is dynamically accessible, or whether there may be other important regions of non-adiabatic coupling. It is also not clear, based on the proposed dissociative transition state, why the non-reactive (E–V) quenching should be the major channel (albeit only by a 60:40 ratio), or why the reactive branching to $MgCH_3^+$ should dominate so strongly over the branching to MgH^+. More detailed and complete theoretical calculations of the

$MgCH_4^+$ potential energy surfaces are necessary before a definitive interpretation of the reaction mechanism in this prototype metal ion–alkane hydrocarbon system can be given. Modelling of the observed photoproduct branching ratio and energy disposal should provide a rigorous test for both *ab-initio* potential energy surfaces, and theoretical molecular dynamics methods.

3.2.2. $CaCH_4^+$

The photodissociation spectroscopy of $CaCH_4^+$ provides an intriguing contrast to $MgCH_4^+$. The analogous $CaCH_4^+$ ($^2E \leftarrow 1\ ^2A_1$) molecular absorption band to the red of the $Ca^+(4p\ ^2P \leftarrow 4s\ ^2S)$ resonance transition shows complex rovibrational structure and no evidence for any reactive quenching in the photodissociation action spectrum [39].

Ab-initio calculations show $CaCH_4^+$ to be weakly bound in a $1\ ^2A_1$ ground state in C_{3v} geometry, with a fairly long Ca^+–C bond ($R_{Ca-C} = 3.60$ Å), with minimal distortion of the CH_4 ligand and a binding energy of about 0.1 eV [39]. The results for the ground state of $CaCH_4^+$ are qualitatively similar to results obtained by Bauschlicher and Sodupe [70] for $MgCH_4^+$ but with appreciably weaker binding and a larger bond length in each state as expected owing to the larger size of Ca^+.

In the lowest excited state, of ^2E character, the equilibrium geometry is also found in C_{3v} symmetry, with a smaller Ca–C bond length ($R_{Ca-C} = 3.01$ Å). The absence of appreciable Jahn–Teller distortion in the excited states of $CaCH_4^+$ is probably due to the stabilization effect of the larger spin–orbit splitting in Ca^+. In a degenerate ^2E state the orbital part of the degeneracy will lead to Jahn–Teller instability if the spin–orbit interaction is small. However, a large spin–orbit coupling will lift the degeneracy, splitting the ^2E state into states of species $^2E_{1/2}$ and $^2E_{3/2}$, and the introduction of vibronic coupling introduces no further splitting [75].

The dominant feature in the photodissociation action spectrum is a progression of doublets. This progression is more clear in the Ca^+–CD_4 isotopomer and the action spectrum for this case is shown in figure 5. The structure was assigned to a progression in the Ca^+–CH_4 or Ca^+–CD_4 intermolecular stretch with spin–orbit doubling in the excited ^2E state. The low-frequency intermolecular bending mode was also observed. The singly excited degenerate vibrational bending mode is dipole forbidden in the Franck–Condon approximation; however, it is of total symmetry species $E + A_1 + A_2$ and it interacts with the nearby non-vibrating $^2E_{3/2}$ origin through a Fermi resonance. The strong vibronic interactions associated with this mode resulted in scrambled intensities throughout the band, complicating the spectral assignment [39].

To confirm the assignments a simulation was carried out for the origin band region including both the vibrational and the rotational contributions [39]. The result of the simulation is shown in figure 6. Spectroscopic constants based on the simulation are summarized in table 2 below. Because of the presence of the strong vibronic interaction, A^{so} and $\Delta G_{1/2}(v_b)$ are the perturbed values. Nevertheless the structural parameters are in good agreement with expected values based either on *ab-initio* calculations or on the results from similar systems.

Based on the observed red shift of the $CaCH_4^+$ band origin relative to $Ca^+(4p\ ^2P_{3/2} \leftarrow 4s^2\ ^2S_{1/2})$ atomic transition energy at 25 340 cm^{-1}, the dissociation energy for the ^2E excited state could be estimated. Using the calculated binding energy for the ground state (about 0.1 eV), the excited-state binding energy was estimated to be about 0.5 eV. This excited-state binding is significantly weaker than that found in the $^2B_{1,2}$ states of $MgCH_4^+$, again indicating minimal chemical interaction in $CaCH_4^+$.

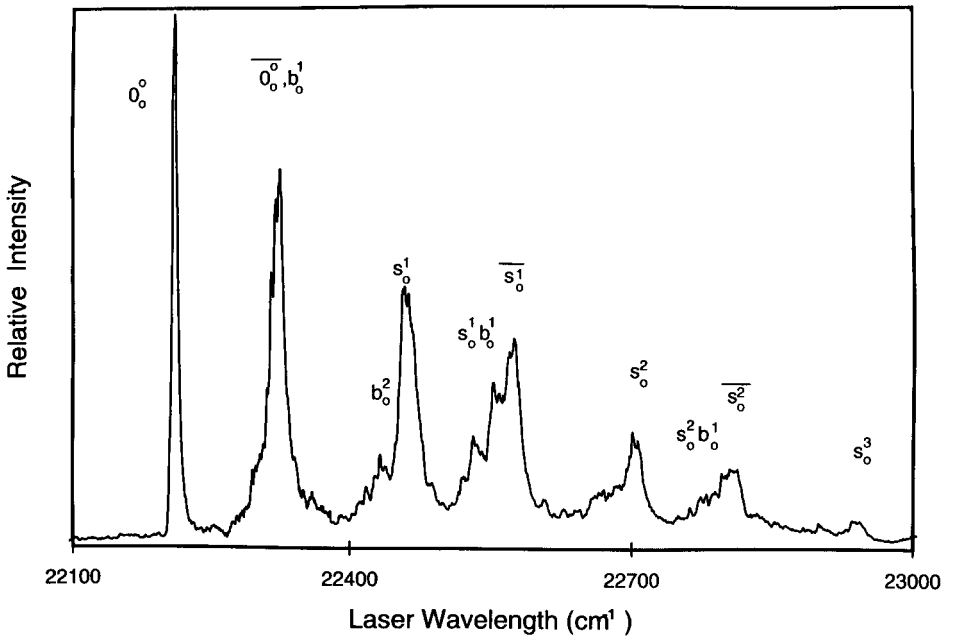

Figure 5. Photodissociation action spectrum of the $^2E \leftarrow {}^2A_1$ transition for $CaCD_4^+$. The vibrational assignments are marked. The unbarred notation corresponds to the $^2E_{1/2}$ component in the excited state, the barred notation corresponds to the $^2E_{3/2}$ component. (From [39].)

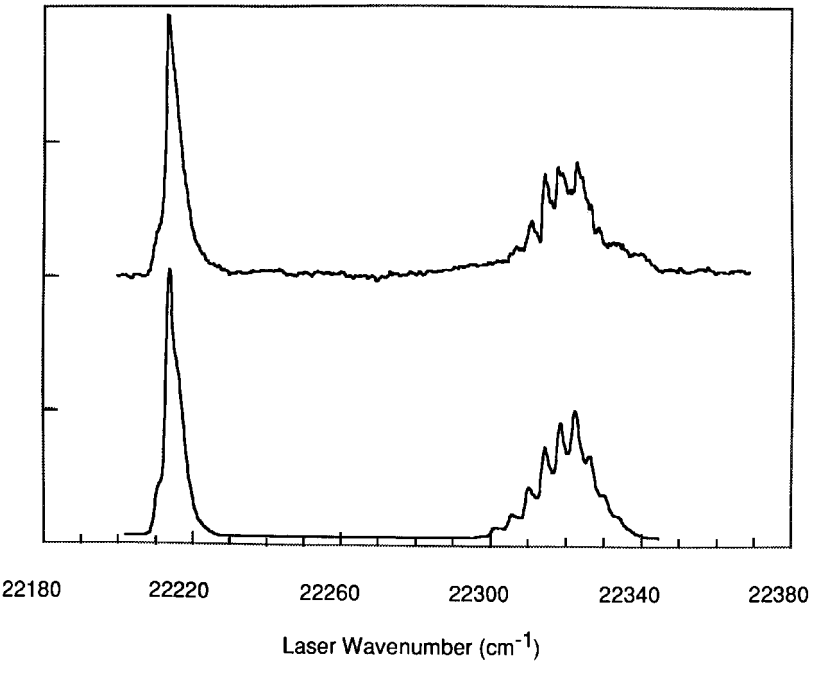

Figure 6. Higher-resolution scan of the first two low-energy bands for the $CaCD_4^+$ $^2E \leftarrow {}^2A_1$ transition: upper trace, experimental; lower trace, simulation. (From [39].)

Table 2. Spectroscopic constants for $CaCH_4^+$ for the $^2E_{1/2} \leftarrow {}^2A_1$ and $^2E_{3/2} \leftarrow {}^2A_1$ bands. Vibrational constants for $CaCD_4^+$ are given in parentheses. (From [39].)

	$1\,^2A_1$		^2E	
	Experimental	Calculated	Experimental	Calculated
T_0 (cm^{-1})	0		22229	20310
A^{so} (cm^{-1})			111	
Ca^+–L stretch (cm^{-1})			270 (244)	
Ca^+–L bend (cm^{-1})			112 (92)	
A (cm^{-1})		5.20		5.09
B (cm^{-1})	0.131	0.111	0.141	0.156
R_{Ca-C} (Å)	3.31	3.60	3.17	3.01

It is interesting to compare spectroscopic data with the previous results from the analogous $MgCH_4^+$ system. The photodissociation spectroscopy of $MgCH_4^+$ showed a broad structureless action spectrum, consistent with a large geometry change on excitation and a rapid dissociation. Chemical reaction to $MgCH_4^+$ and MgH^+ was found to be a major quenching channel, with about 40% branching. In this $CaCH_4^+$ case, the photodissociation action spectrum shows pronounced rovibrational structure, indicating a long-lived excited-state intermediate complex, with no observable reaction yield.

There are a number of factors which may contribute to the slow dissociation rate and the low reactive quantum yield in the $CaCH_4^+$ case. For example, steric hindrance effects may limit the dissociation rate in the $CaCH_4^+$ case. Mg^+ is smaller than Ca^+ and may more effectively approach the C–H bond. This close approach allows for more efficient orbital overlap and transfer of electron density from the Mg^+ 'p' orbital to the antibonding lower unoccupied molecular orbital (LUMO) centred on the C–H bond. Because of the larger size of Ca^+, it may hindered from close approach to the C–H bond, resulting in less orbital overlap and electron transfer. The excited intermediate will be less distorted, and the ground and excited-state surfaces may not significantly interact, leading to a lower non-adiabatic coupling rate. This argument is supported by the spectroscopic data and by the *ab-initio* calculations which show the $CaCH_4^+$ complex to be fairly weakly bound at long range and with minimal distortion of the CH_4, in both the ground state and the first excited states. In addition to possible steric effects, the energetics and differences in the electronic structure (especially the presence of the 3d orbitals in Ca^+) are also likely to be significant and may play an important role in the dissociation.

The importance of steric effects in controlling the quenching of excited neutral metal atoms by alkanes has also been emphasized by Breckenridge [44]. For example, it is interesting to note that laser spectroscopy studies of neutral Cd–CH_4 van der Waals complexes have shown that these species are also essentially van der Waals bound behind a substantial activation barrier to reaction in the excited $Cd^*(^3P)CH_4$ states [76]. Again, this is thought to be due to steric hindrance effects limiting the approach to insertion.

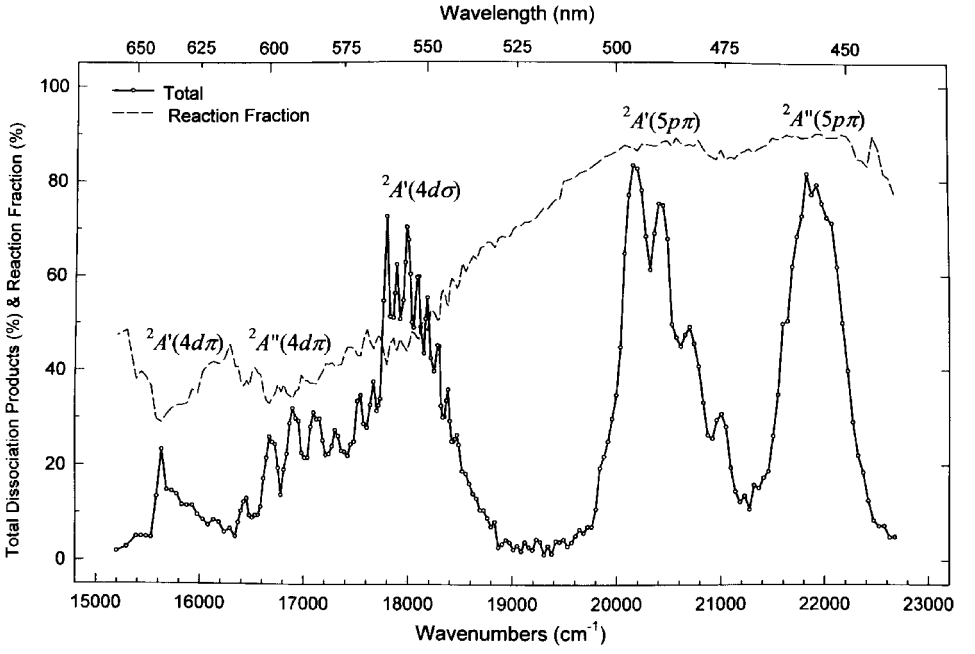

Figure 7. Total photodissociation cross-section for $Sr^+(CH_3OH)$ in the photon energy region from 15000 to 23000 cm^{-1}. The reaction fraction, that is the fraction of dissociation products corresponding to $SrOD^+$ products, is also indicated. Electronic state assignments are indicated for the band systems. (Taken from [27] with permission from the author.)

3.3. *Photoactivation of C–O bonds*

3.3.1. MCH_3OH^+ ($M = Mg$ *on* Sr)

Duncan and co-workers [28] have reported preliminary survey measurements on the photodissociation of $MgCH_3OH^+$ at selected wavelengths in the near UV. They observed a number of reactive and non-reactive quenching products including Mg^+, $MgOH^+$, MgO^+ as well as charge-transfer (CT) products CH_3OH^+ and CH_3^+, depending on the excitation wavelength.

More extensive spectroscopy studies have been reported for $SrCH_3OH^+$ by the research group of Farrar [27]. They have identified five distinct absorption bands in the visible (430–670 nm), correlating with the $Sr^+(5s–4d)$ and $Sr^+(5s–5p)$ atomic transitions. The observed photodissociation channels in this spectral region are

$$SrCH_3OH^+ + h\nu \rightarrow (SrCH_3OH^+)^* \rightarrow Sr^+ + CH_3OH, \tag{3.12}$$

$$\rightarrow SrOH^+ + CH_3. \tag{3.13}$$

Ab-initio calculations on $MgCH_3OH^+$ and on SrH_2O^+ by Bauschlicher and co-workers [77, 78] have been carried out. In each case the bimolecular complex is strongly bound by electrostatic ion–dipole forces with the metal ion attached to the O atom. While calculations on the analogous $SrCH_3OH^+$ complex have not been reported, it probably has a similar binding geometry.

The total photodissociation action spectrum for $SrCH_3OD^+$ is shown in figure 7 as the solid curve; the reaction fraction is shown as the broken curve [27]. The reaction yield generally increases from about 40% to about 90% with photon energy, although at the highest energies probed there may be evidence for a slight turn-down in the

reaction probability. In comparison with the previous results for the reactive quenching of Mg^+ by D_2 and CH_4, it is interesting and surprising that there does not appear to be any significant electronic orbital alignment effect in the reaction rate or in the reaction yield in this system.

The two highest energy bands are assigned to the excitation of the $^2A'(5p\pi)$ and $^2A''(5p\pi)$ states in C_s symmetry, with reactive quenching dominating. The vibrational structure is not well resolved in these bands but a progression in the Sr^+–O intermolecular stretch has been identified with $\omega_e \approx 300$ cm^{-1} in $SrCH_3OD^+$.

More extensive vibrational structure is observed in the lower-energy bands which are assigned as transitions to the $^2A''(4d\pi)$, $^2A''(4d\pi)$ and $^2A'(4d\sigma)$ states. A clear progression in the Sr^+–O stretch is identified in both the $^2A''(4d\pi)$ and the $^2A'(4d\sigma)$ states of $SrCH_3OD^+$, with $\omega_e \approx 270$ cm^{-1} and $\omega_e \approx 190$ cm^{-1} respectively. Additional mode structure with a spacing of about 95 cm^{-1} in the $^2A'(4d\sigma)$ state is tentatively identified with the out-of-plane wagging motion.

One of the most intriguing results from this study is the observation of clear structure in the reactive quantum yield which was *anti*correlated with the observed vibrational resonances [27]. Such an effect might be expected if there are two competing processes which take place on vastly different time scales. Rapid dissociation due to internal conversion or pre-dissociation can lead to a lifetime-broadened continuum in the photodissociation action spectrum as seen in both MgD_2^+ and $MgCH_4^+$. If, in addition, there are overlapping quasibound resonance states which are selectively coupled to the reactive quenching channel, these states can reduce the reaction rate while the rate of non-reactive dissociation remains unchanged. The observed variation in the reactive to non-reactive branching ratio is consistent with this suggestion.

The chemical reaction pathway (3.13) is not well understood for the MCH_3OH^+ clusters, although it may involve a C–O bond-stretch quenching process. In this regard it is worth noting that the photoinitiated activation of C–O bonds has also been observed in $MgCO_2^+$ and $CaCO_2^+$ by the research group of Duncan [31] and in the metal dimer system, $Mg_2CO_2^+$ in our laboratory [34]. In each case the bimolecular complex is bound in linear geometry by ion–quadrupole electrostatic forces. In the $CaCO_2^+$ case it has been proposed that reaction from the excited Π state of the complex proceeds through insertion into the C–O bond; back donation of electron density from the Ca^+ '$p\pi$' orbital into the antibonding $2\pi_u$ LUMO of CO_2 can lead to a bending of the CO_2 which would facilitate the rearrangement necessary for insertion [31]. The linear equilibrium geometry of the complex is favourable for this π–π^* molecular orbital overlap.

Photoexcitation of the analogous $^2\Pi \leftarrow 1\ ^2\Sigma^+$ molecular band in $MgCO_2^+$ results only in non-reactive dissociation to Mg^+. It is possible (although not known) that reaction in this case may be energetically unfavourable. Remarkably, however, photoinitiated C–O bond chemistry was observed in $MgCO_2^+$ following excitation of the repulsive $3p\sigma\ ^2\Sigma^+$ state [31]! The reaction mechanism in this case is not *a priori* obvious; while an insertion mechanism was proposed, the molecular orbital overlap (σ–π^*) does not seem favourable. Overall the dynamical mechanism for metal ion attack on the C–O bonds is not as well understood as for the examples of H–H and C–H bond activation.

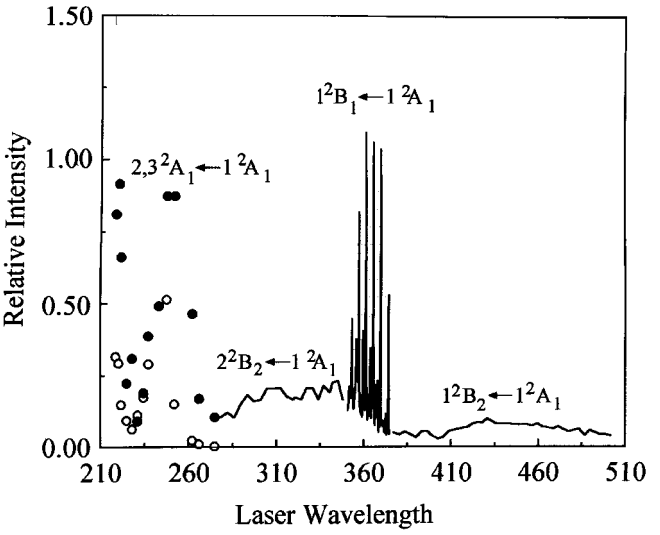

Figure 8. UV–visible photofragmentation action spectrum for $MgC_2H_4^+$, where the wavelength is given in nanometres and, in the spectral range below 265 nm, only a pointwise spectrum was obtained: (●), Mg^+; (○), $C_2H_4^+$. (From [41].)

3.4. *Photoactivation of C–C bonds*

3.4.1. $MgC_2H_4^+$

The importance of π-bonded metal ion–hydrocarbon complexes in inorganic and organometallic chemistry has been recognized since the pioneering work of Mulliken [79]. $MgC_2H_4^+$, studied in our laboratory, is one of the simplest examples of such a π-bonded complex. In the $MgC_2H_4^+$ ion–molecule complex, the UV–visible spectroscopy is complicated because metal-centred transitions, ligand-centred transitions and CT processes are all important [40, 41]. These processes lead to overlapping bands and the electronic states are strongly mixed. The situation is common in the spectroscopy of organometallics, particularly in solution, where spectral band assignments are often uncertain.

Figure 8 shows the UV–visible fragmentation action spectrum for $MgC_2H_4^+$. Five distinct $MgC_2H_4^+$ molecular absorption bands in the visible–UV (550 nm $> \lambda >$ 218 nm) were observed, with the assignments as noted in the figure [41]. Mg^+ was the major photofragment observed over the entire spectral range. No reactive products were observed, although for $\lambda <$ 270 nm a 30–40% branching to the CT product $C_2H_4^+$ was also apparent. The possible photofragmentation processes leading to the observed products can be described as

$$MgC_2H_4^+ + h\nu \rightarrow (MgC_2H_4^+)^* \rightarrow Mg^+(3\,^2S) + C_2H_4(^1A_g), \quad (3.14)$$

$$\rightarrow Mg^+(3\,^2S) + C_2H_4{}^*(a\,^3B_{1u}/^3A_2), \quad (3.15)$$

$$\rightarrow Mg(3\,^1S) + C_2H_4^+(^2B_3), \quad (3.16)$$

$$\rightarrow Mg^+(3\,^2P) + C_2H_4(^1A_g), \quad (3.17)$$

$$\rightarrow Mg(3\,^3P) + C_2H_4^+(^2B_3). \quad (3.18)$$

Spectral assignments were based in part on the results from *ab-initio* electronic structure calculations [40, 41, 80]. Sodupe and Bauschlicher [80] have carried out *ab-initio* calculations of the electronic structure of $MgC_2H_4^+$. The $MgC_2H_4^+$ complex is fairly strongly bound ($D_0'' =$ 0.806 eV by the modified coupled pair functional–self-

Table 3. Comparison of the observed transition wavelengths for $MgC_2H_4^+$ with *ab-initio* predictions or the vertical excitation wavelength. (From [41].)

Transition	Observed wavelength (nm)	Calculated vertical excitation wavelength (nm)
$1\ ^2B_2 \leftarrow 1\ ^2A_1$	400–500	427
$1\ ^2B_1 \leftarrow 1\ ^2A_1$	353–374	366
$2\ ^2B_2 \leftarrow 1\ ^2A_1$	270–380	282
$2\ ^2A_1 \leftarrow 1\ ^2A_1$	231–270	246
$3\ ^2A_1 \leftarrow 1\ ^2A_1$	< 231	202

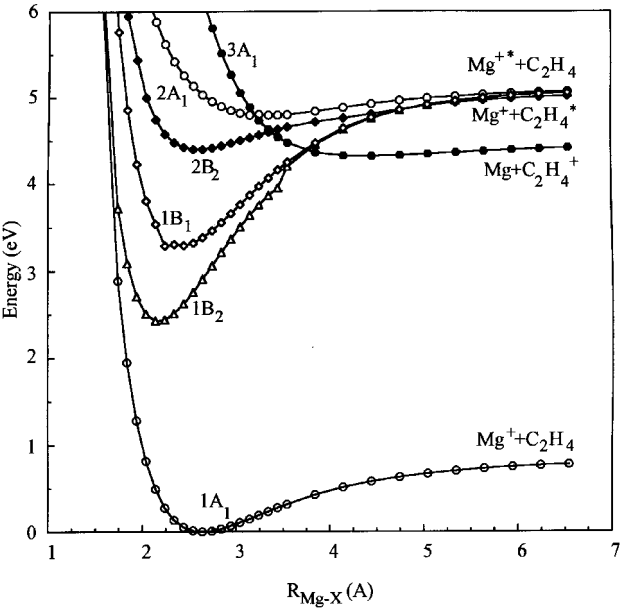

Figure 9. *Ab-initio* potential surface scans for $MgC_2H_4^+$ along the R_{Mg-X} dissociation coordinate. All states are doublet spin symmetry. (See [41] for details.)

consistent field method), in an equilibrium structure with Mg^+ lying atop C_2H_4 in C_{2v} symmetry. The Mg^+–C_2H_4 equilibrium bond distance (measured to the midpoint of the C=C bond) is 2.547 Å. The ethylene moiety is relatively undistorted, with a C=C bond length of 1.343 Å.

Sodupe and Bauschlicher [80] also identified three low-lying electronically excited states with $Mg^+(3p)$ parentage: $1\ ^2B_2$, $1\ ^2B_1$ and $2\ ^2A_1$ [80]. For the attractive states of $^2B_{1,2}$ symmetry the Mg^+ 'p' orbital is aligned either parallel to the C=C bond ($^2B_2$), or perpendicular to the C–Mg–C plane ($^2B_1$). A third molecular state, $2\ ^2A_1$, correlating with Mg^+*(3p) lies at higher energy; this state is essentially repulsive with the Mg^+ 'p' orbital lying in the C–Mg–C plane and perpendicular to the C=C bond.

In order to include the important CT states and to facilitate the band assignments these calculations were extended to higher energies using both CIS and complete-active-space self-consistent field (CASSCF) methods in the Gaussian '94 platform [41]. Five spin doublet excited states of $MgC_2H_4^+$ were found in the relevant energy

range. In agreement with Sodupe and Bauschlicher, three electronically excited states ($1\ ^2B_2$, $1\ ^2B_1$ and $2\ ^2A_1$) with predominantly $Mg^+(3p\ ^2P)$ parentage were identified. Results for the ground-state structure and these excited states were in good agreement with the calculations by Sodupe and Bauschlicher [80]. Two additional excited states were identified in this region as $2\ ^2B_2$ and $3\ ^2A_1$. The $2\ ^2B_2$ state of the complex is an ethylene-centred excited state (correlated to the $a\ ^3B_{1u}$ state of C_2H_4 in D_{2h} planar symmetry), mixed with CT character. The $3\ ^2A_1$ state is nominally a metal-to-ligand CT state arising from the $Mg(3s)–C_2H_4^+$ parent. However, this state is also strongly coupled to the nearby $2\ ^2A_1$ state. Thus, it is important to recognize that these nominal correlations are not rigorous; the electronically excited states all show evidence for strong coupling with nearby states of the same symmetry. The resultant potential energy curves for $MgC_2H_4^+$ along the R_{Mg-X} dissociation coordinate are shown in figure 9. Except for the R_{Mg-X} distance, all the other geometric parameters have been fixed at their equilibrium values.

Based on these theoretical predictions, the lowest two energy bands $1\ ^2B_2 \leftarrow 1\ ^2A_1$, $1\ ^2B_1 \leftarrow 1\ ^2A_1$ could be straightforwardly assigned to transitions correlated to the metal-centred $Mg^+(3p\pi \leftarrow 3s\sigma)$ resonance excitation, with the different symmetry states corresponding to the distinct alignments of the Mg^+ 'p' orbital with respect to the C=C bond in ethylene. The lowest-energy band, corresponding to excitation of the $1\ ^2B_2$ state, consists of a broad and structureless continuum, indicative of a large geometry change on excitation and a fast pre-dissociation. The next band, corresponding to excitation of the $1\ ^2B_1$ state shows pronounced vibrational structure. This situation is quite reminiscent of the spectra in figure 3 for MgD_2^+, suggesting that the photodissociation mechanisms in these two cases are similar.

One of the remaining bands was assigned as the predominantly ethylene-centred transition $2\ ^2B_1 \leftarrow 1\ ^2A_1$ correlated to a highly forbidden excitation in C_2H_4 ($a\ ^2B_{1u} \leftarrow X\ ^1A_g$, in D_{2d} symmetry), with mixed CT character. The shortest wavelength bands were assigned as transitions to the $2\ ^2A_1$ and $3\ ^2A_1$ states. As noted above, these states can be nominally identified with an $Mg^+(3p\sigma)$ excited state ($2\ ^2A_1$) and a metal-to-ligand CT state ($3\ ^2A_1$) but are, in fact, of mixed character. A comparison of the observed band positions with the *ab-initio* predictions for the vertical excitation wavelengths is given in table 3. In this section we concentrate on the lower-energy bands involving transitions to the lowest three 'bound' electronically excited states and shall postpone discussion of the spectroscopy of the CT state to the next section.

3.4.1.1. $MgC_2H_4^+(1\ ^2B_2 \leftarrow 1\ ^2A_1)$. It is intriguing that excitation to the deeply bound $1\ ^2B_2$ state resulted in no discrete vibrational structure at all. The lack of observable structure in the $1\ ^2B_2 \leftarrow 1\ ^2A_1$ band is the result of significantly greater spectral complexity in the upper state due to a large geometry change, coupled with lifetime broadening consistent with a rapid pre-dissociation process. In this spectral range, excited-state channels are not energetically open, and dissociation must involve a non-adiabatic transition to the ground-state surface.

We have discussed similar results in both MgD_2^+ and $MgCH_4^+$ photodissociation above. In each of those cases, pre-dissociation of the $1\ ^2B_2$ surface was argued to be fast, proceeding through a bond-stretch mechanism. An analogous mechanism has been postulated here, however, this case involves the activation of the C=C π bond rather than H–H or C–H σ bonds. The calculated minimum energy geometry for the $^2B_2$ surface shows a clear trend toward Mg^+ insertion into the C=C bond with a contraction of the $Mg^+–C_2H_4$ distance from 2.63 to 2.11 Å, accompanied by a stretch

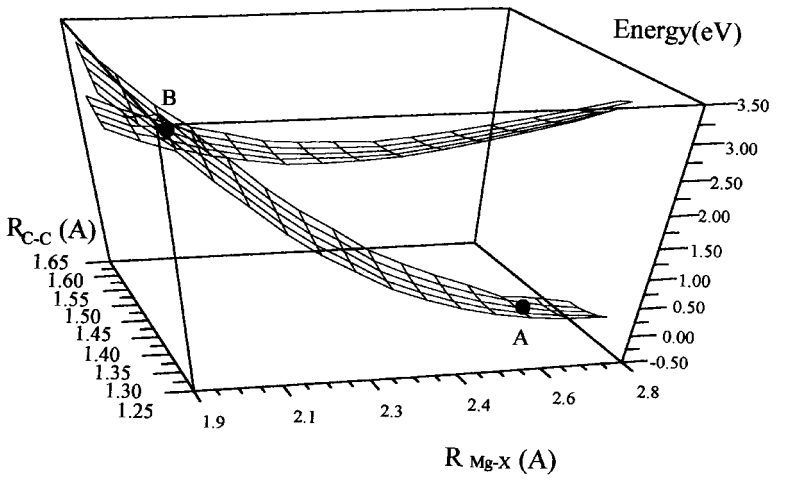

Figure 10. $1\,^2B_2$-$1\,^2A_1$ surface crossing seam in C_{2v} symmetry for $MgC_2H_4^+$ by a state averaged CASSCF calculation. Point A represents the ground-state equilibrium geometry and point B identifies the conical intersection. (See [41] for details.)

in the C=C bond from 1.34 to 1.46 Å. The geometry of the $^2B_2$ state is favourable for the molecular orbital overlap between the Mg^+ 'p' orbital and the lowest π^* antibonding orbital on C_2H_4, and this overlap is enhanced by the C=C bond stretch. This distortion gives rise to a conical intersection with the ground electronic surface, which, as in MgH_2^+, opens an efficient pathway for quenching. In this case, however, the C=C bond is much stronger and is not nearly 'broken' by the interaction.

Ab-initio calculations on the Gaussian '94 platform found evidence for such a conical intersection near the $^2B_2$ minimum for $MgC_2H_4^+$ [41]. A further reactive path calculation showed that the excited complex can relax to the conical intersection without encountering any significant barrier. These results are shown in figure 10. This bond-stretch mechanism is essentially similar to that proposed for the dissociation of MgH_2^+ and $MgCH_4^+$, following activation of the H–H or C–H σ bonds, and the results for $MgC_2H_4^+$ suggest that the mechanism is also significant for π-bonded systems involving the activation of C=C bonds.

While C=C bond breaking is not energetically possible in this spectral range, C–H bond breaking channels are expected to be open for $\lambda < 470$ nm. However, the Mg^+–C_2H_4 equilibrium distance in the $^2B_2$ state is large enough that, in C_{2v} symmetry, there is minimal chance for overlap with the orbitals localized on an individual C–H bond. Non-reactive (E–V) energy transfer therefore dominates the quenching.

3.4.1.2. $MgC_2H_4^+(1\,^2B_1 \leftarrow 1\,^2A_1)$. For the $1\,^2B_1$ state a fast coupling to the ground-state surface is prohibited by symmetry since in C_s geometry the $1\,^2B_1$ state is of A″ character while the ground state is A′. Consistent with this, the $1\,^2B_1 \leftarrow 1\,^2A_1$ transition in the near UV showed pronounced vibrational structure indicative of a long-lived complex. The spectrum shows a clear progression in the Mg^+–C_2H_4 intermolecular stretch. Analysis of the vibrational spectrum also provided evidence for activity in the intermolecular bend and in an intramolecular ethylene umbrella mode [40, 41].

Table 4. Spectroscopic constants for $MgC_2H_4^+$ for the $1\ ^2B_1 \leftarrow 1\ ^2A_1$ band. (From [41].)

	$1\ ^2A_1$		$1\ ^2B_1$	
	Experimental [41]	Calculation [80]	Experimental [41]	Calculation [80]
T_{00} (cm^{-1})	0	0	26716	26807
$Mg^+-C_2H_4$ stretch ω_2[a] (cm^{-1})			329	335
$Mg^+-C_2H_4$ out-of-plane wag ω_3 (cm^{-1})			439	258
CH_2-CH_2 wag ω_7 (cm^{-1})			1024	1078
D_0 (eV)	0.7	0.806	1.84	1.91

[a] The observed intermolecular stretch anharmonicity parameter is $x_{22} = -2.3\ cm^{-1}$.

The strongest progression in the spectrum was assigned to $2_0^{v'}$ with $v' = 0$–6, where ν_2 is the $Mg^+-C_2H_4$ intermolecular stretch mode (with a_1 symmetry) in the upper state $1\ ^2B_1$. The activity of this intermolecular stretch is consistent with the expected shortening of the $Mg-C_2H_4$ bond distance in the excited state [40, 41].

Another weaker and shorter progression was assigned to the combination band $2_0 3_0^1$. The $Mg^+-C_2H_4$ intermolecular out-of-plane wag ν_3 is of b_1 character. An additional higher-energy mode is also present in the spectrum and must be associated with an intramolecular mode of ethylene. It is assigned as a progression built on the CH_2-CH_2 wag (ν_7 mode of a_1 character), $2_0 7_0^1$. Note here that excitation of the metal-centred absorption band of the complex activates one of the *intra*molecular modes of the ethylene ligand. Such an effect has also been previously observed in $Mg-N_2^+$ and demonstrates that, in favourable cases, it should be possible to extract information about the distortion of the molecular ligand in the complex through an analysis of shifts in the intramolecular vibrational modes [30]. The specific assignment for these latter weaker modes is more ambiguous owing to the limited number of peaks in the spectrum and the complexity of the $MgC_2H_4^+$ molecule, which has a total of 15 vibrational modes. The spectroscopic constants for this vibrational assignment are given in table 4, in comparison with the *ab-initio* predictions [40, 41, 80].

3.4.1.3. $MgC_2H_4^+(2\ ^2B_2 \leftarrow 1\ ^2A_1)$. The $2\ ^2B_2 \leftarrow 1\ ^2A_1$ transition is based primarily on the $a\ ^3B_{1u} \leftarrow X\ ^1A_g$ spin-forbidden transition in the C_2H_4 monomer in D_{2h} symmetry. This band is extremely weak in isolated C_2H_4 and was first observed by Reid [81] in long-path absorption spectroscopy in liquid ethylene. The observed photofragmentation cross-section for this band in the $MgC_2H_4^+$ complex, however, was comparable with those for the strong Mg^+-centred transitions. This dramatic enhancement probably results from coupling with other nearby states of the same symmetry including both the Mg^+-centred excited state, $1\ ^2B_2$, and the excited CT state arising from $Mg^*(3p)-C_2H_4^+$. In addition the spin selection rules are relaxed in the complex owing to angular momentum coupling with the open-shell Mg^+ ion. The strong enhancement of a forbidden ligand transition in the cluster environment suggests that such forbidden transitions may be more important in the cluster environment than previously recognized [41].

It is interesting that no bound-state structure was observed for this state. The lack of vibrational structure is thought to be due to the spectral complexity associated with a large geometry change in C_2H_4 in this $\pi^* \leftarrow \pi$ transition. Isolated ethylene is found

in the X ^1A_g ground state to have a planar D_{2h} symmetry. However, the a $^3B_{1u}$ excited state (D_{2h} symmetry) relaxes to $^3A_2$ in D_{2d} symmetry, with a near-90° twist about the C=C bond [82]. The lack of observable structure may also be due in part to the spectral overlap with the 1 $^2B_1 \leftarrow 1\ ^2A_1$ band. The low-energy limit of the 2 $^2B_2 \leftarrow 1\ ^2A_1$ band probably overlaps the heavily congested high-energy portion of the 1 $^2B_1 \leftarrow 1\ ^2A_1$, making it difficult to resolve or definitely to identify any 2 $^2B_2$ state structure in that region.

3.5. *Charge-transfer photochemistry*

3.5.1. *M^+–benzene and M^+–acetone ($M^+ = Mg^+, Al^+, Ag^+, Fe^+, Cu^+$, etc.)*

Duncan and co-workers [32] have carried out extensive studies of photoinduced CT chemistry in a series of π-bonded metal ion–hydrocarbon complexes using photodissociation spectroscopy. Metal-to-ligand CT processes are of vital importance in inorganic and organometallic photochemistry in solution but are often complicated by bulk effects and the presence of competing processes. The photodissociation spectroscopy of isolated metal ion–ligand complexes in the gas phase affords the opportunity to study the metal–ligand bonding and the fundamental CT dynamics in detail.

The nominal CT band position can be estimated from the difference between the ionization potentials of the neutral metal atom and the hydrocarbon ligand: IP(M)− IP(L). However, the photoinduced CT bands are commonly found to be very blue shifted from this value, often by a few electronvolts [32]. In these systems, the metal ion typically has a much lower ionization potential than the hydrocarbon ligand and the charge in the ground state will be localized predominantly on the metal centre. Because the polyatomic ligand often has a significant polarizability, the complexes can be relatively strongly bound by electrostatic forces in the ground state. In the CT excited state of character $M-L^+$; however, the metal atom is generally less polarizable, and the charge is often more delocalized over the ligand, leading to a weaker and longer-range electrostatic bond in the excited state. This results in an expected blue shift in the CT band position [32].

Following photoexcitation in the CT band, the expected dissociation pathways are:

$$(M^+-L) + h\nu \rightarrow (M-L^+)^* \rightarrow M + L^+ \quad \text{(CT dissociation)}, \tag{3.19}$$

or

$$\rightarrow M^+ + L \quad \text{(direct dissociation)}. \tag{3.20}$$

Channel (3.19) corresponds to direct dissociative CT. Dissociation through channel (3.20) may be observed when the photoexcitation is to quasibound CT states of the complex which lie below the $M + L^+$ asymptote. Such 'frustrated' CT dissociation can result from internal conversion or pre-dissociation to lower-lying surfaces, accompanied by reverse CT, a process which is common in organometallic photochemistry in solution. Metal-centred excitation to repulsive states which leads to direct dissociation of the electrostatic bond may also be possible [32]. In clusters with larger hydrocarbons, more complex chemical dissociation processes are seen. For example, in the dissociation of Mg^+-acetone channels (3.19) and (3.20) (to CH_3CO^+ and Mg^+ respectively) are observed but, in addition, $MgCH_3^+$ photoproduct, ascribed to photochemistry localized within the acetone moiety, has also been detected [28]. Developing a detailed theoretical understanding of these more complicated processes will present an interesting challenge to molecular dynamicists.

CT bands are normally broad and structureless and present little structural information. However, it is possible to place an upper limit on the ground-state dissociation energy

$$D_0'' \leqslant h\nu(\mathrm{CT}) - [\mathrm{IP(M)} - \mathrm{IP(L)}].$$

In cases where a threshold for direct dissociative CT is observed, the threshold wavelength can give a limit which is close to the actual bond energy [32]. If the photodissociation kinetic energy release can be measured, this limit can be further tightened as in the $MgC_2H_4^+$ system discussed below [41]. Accurate experimental bond dissociation energies in M^+–L complexes are crucial to developing a full understanding of the bonding in organometallic complexes.

3.5.2. Mg^+–C_2H_4

In most of the systems investigated by Duncan and co-workers [32] the CT bands were resolved from other molecular bands of the complex. In the $MgC_2H_4^+$ ion–molecule complexes studied in our laboratory, the UV–visible spectroscopy is complicated because metal-centred transitions, ligand-centred transition and CT processes are all important and the electronically excited states are of mixed character as discussed in section 3.4 above [40, 41].

Dissociation through the repulsive $2\,^2A_1$ and $3\,^2A_1$ states of $MgC_2H_4^+$ at the shortest wavelengths is expected to be direct, leading primarily to the ion products Mg^+*(3p) or $C_2H_4^+$ (figure 9). The transitions (2, 3) $^2A_1 \leftarrow 1\,^2A_1$ in the short-wavelength region 230–270 nm have mixed metal-centred and CT character. This is consistent with the observation that $C_2H_4^+$ was observed throughout both bands, with a roughly constant branching of 30–40% [41]. Consequently, these bands are discussed together.

As noted above, the observed wavelength threshold in figure 8 for dissociation to $C_2H_4^+$ photoproduct ($\lambda \approx 270$ nm) can be used to place a crude upper limit on the Mg^+–C_2H_4 bond dissociation energy. This leads to an estimate which is significantly larger than the *ab-initio* value of about 0.8 eV owing to the large kinetic energy release in the dissociation. Indeed the large kinetic energy release in the CT product channel is readily apparent in a broadened flight-time profiles for $C_2H_4^+$ as shown in figure 11 for a photolysis wavelength of 246 nm [41]. The observed flight-time profile can be inverted to give information about the photofragment kinetic energy distribution function and the anisotropy parameter as discussed in section 2. The result of the simulation of the flight-time profile is also shown.

The observed flight time profiles showed a photofragment anisotropy consistent with a parallel $^2A_1 \leftarrow {}^2A_1$ transition, as expected. However, the effective anisotropy parameter, $\beta = +1$, obtained from a simulation of the flight-time profile, was much less than the limiting value of $\beta = +2$, expected from a direct CT dissociation through channel (3.16) [41]. The most likely reason for a depressed anisotropy is the presence of a second indirect dissociation mechanism in this spectral region, although the exact nature of this process is not yet fully understood [41].

The kinetic energy distribution function was broad, indicating appreciable energy loss into the ethylene ligand. This is also consistent with the involvement of a second dissociation mechanism. The end-point kinetic energy (or maximum kinetic energy, corresponding to minimal loss of energy into vibration of the ethylene ion fragment), was determined from the flight-time broadening and could be used for determining the bond dissociation energy from

$$D_0'' = h\nu - [\mathrm{IP}(C_2H_4) - \mathrm{IP(Mg)}] - \mathrm{KER(max)}.$$

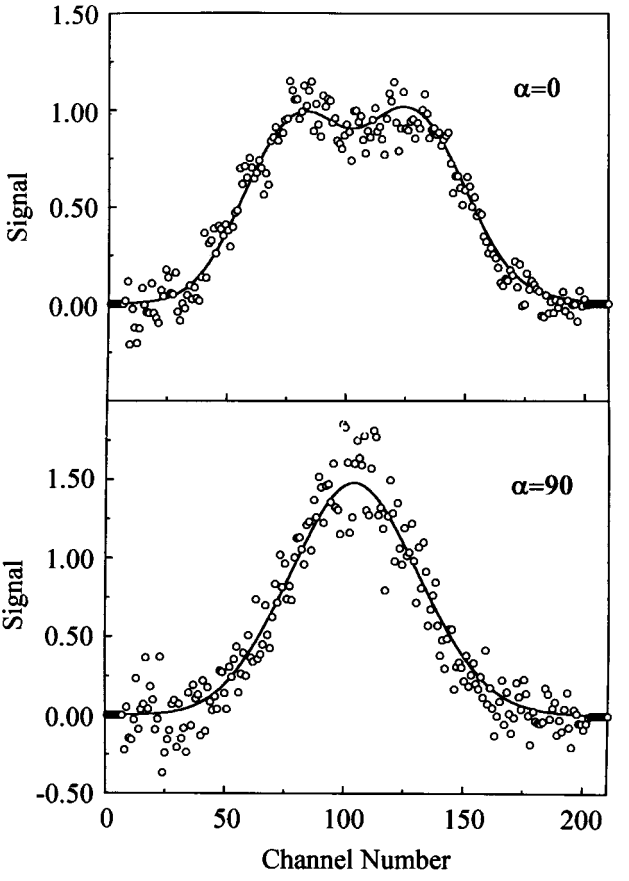

Figure 11. Time-of-flight profiles for $C_2H_4^+$ photofragment from the CT dissociation of $MgC_2H_4^+$, showing a clear photofragment anisotropy. The simulation is given as the smooth curve. (See [41] for details.)

This analysis gave an experimental value of $D_0'' = 0.7 \pm 0.2$ eV in good agreement with the MCPF bond dissociation energy ($D_0'' = 0.806$ eV) of Sodupe and Bauschlicher [80]. Combining this result with the spectroscopic value for ν_{00} in the 1 $^2B_1$ excited state, the bond dissociation energy for this state could be determined:

$$D_0'(1\,^2B_1) = [E(Mg^+(3p)) - E(Mg^+(3s))] + D_0'' - \nu_{00} = 1.8 \pm 0.2 \text{ eV},$$

also in very good agreement with *ab-initio* values ($D_0'(1\,^2B_1) = 1.91$ eV) [80].

As noted above, there is strong evidence in the ethylene ion photofragment kinetic energy distribution and anisotropy for a second dissociation channel that competes effectively with direct CT dissociation through channel (3.16). The presence of such a process is confirmed by the observation that the major branching at 246 nm is to the Mg^+ product. This is remarkable because excitation a this wavelength is appreciably below the energy threshold for direct dissociation to $Mg^+(3p) + C_2H_4$! This means that the Mg^+ fragment must result from coupling onto a lower-energy potential surface and dissociation to channel (3.15) or channel (3.14). Even in this small bimolecular complex and in the absence of a solvent cage, this process must be fast enough to compete with direct CT dissociation. While the details of this process are still under investigation it is clear that photodissociation spectroscopy, in concert with trans-

lational energy spectroscopy of the photofragments, offers a unique opportunity to probe the fundamental dynamics of the CT process.

4. Summary

The photodissociation spectroscopy of weakly bound bimolecular complexes has proven an effective technique for the detailed investigation of metal ion–hydrocarbon interactions. In many of the examples we have discussed, bound–quasibound-state spectroscopy has been effectively used to determine the structure of the metal ion–hydorcarbon bimolecular complex. The intermolecular vibrational modes are usually active and dominate the vibronic spectrum, giving a quantitative measure of the metal–ligand bonding interactions. We have also seen that photoexcitation of the metal-centred absorption bands of the complex can activate the intramolecular modes of the hydrocarbon ligand. In some cases, this may give information about how the internal structure of the hydrocarbon is altered in the complex. Information about the rotational state structure of the complex has also been obtained, in favourable cases, either through a simulation of the observed rotational contours, or through rotationally state resolved measurements. Even in cases where detailed vibronic structure is not observed, photoinduced CT dissociation can often give quantitative information about metal ion–ligand bond energies. If photodissociation spectroscopy is coupled with kinetic energy spectroscopy of the products, accurate bond dissociation energies can be possible. Metal ion–hydrocarbon interactions are of fundamental and vital importance in many fields of chemistry and physics, and photodissociation spectroscopy experiments, coupled with *ab-initio* electronic structure calculations, give detailed and quantitative information about these essential interactions.

The photodissociation of the weakly bound precursor complex also serves to mimic a bimolecular half-collision. Photodissociation spectroscopy, in concert with translational energy spectroscopy of the photofragments, can give clear insight into the metal ion–hydrocarbon chemical dynamics. We have discussed examples of the photoactivation of H−H and C−H σ bonds, and C−O bonds, leading to very ***efficient but non-adiabatic*** reactive dissociation of the complex. In $MgC_2H_4^+$, where reactive channels are less accessible owing to the strength of the C=C double bond, we have also seen evidence for the photoactivation of the C=C π bond, resulting in rapid non-reactive dissociation through a non-adiabatic pathway. These processes represent the half-collision analogue of the molecular quenching of excited Mg^+ through chemical reaction or through E–V energy transfer.

In the side-on (C_{2v}) attack by $Mg^+(3p)$ on the D−D σ bond in D_2, and on the C=C π bond in ethylene, there is a pronounced alignment effect on the non-adiabatic quenching rate. The state of $^2B_2$ symmetry (with the Mg^+ p orbital aligned parallel to the bond under attack) is quenched very rapidly so that no vibrational structure is seen in the spectrum. The state of $^2B_1$ symmetry, on the other hand (with the Mg^+ p orbital aligned out of the plane of attack) is quenched slowly, and a resolvable vibrational (and even rotational) resonance structure is apparent in the dissociation action spectrum. In each case, excitation of the state of $^2A_1$ symmetry (with the Mg^+ 'p' orbital directed towards the bond under attack) results in direct dissociation in the Mg^+–ligand coordinate. These pronounced alignment effects, coupled with the results from *ab-initio* electronic structure calculations give a clear picture of the chemical dynamics. Dissociation on the $^2B_2$ surface follows through a bond-stretch mechanism in near-C_{2v} symmetry, facilitated by the good molecular orbital overlap between the Mg^+ p orbital and the antiboding orbitals of the molecular ligand in this geometry.

The bond-stretch process leads to a conical intersection in $^2A'$ symmetry which allows a pathway for an efficient non-adiabatic transition to the ground-state surface.

In the case of $Mg^+(3p)$ attack on the C–H bond of methane, alignment effects are not as readily apparent owing to a large geometry change in the complex following the radiative excitation. Nevertheless, the spectroscopic data, supported by preliminary *ab-initio* results, indicates a similar bond-stretch quenching mechanism in this case. Furthermore, there is evidence that steric hindrance effects may play a significant role in the chemical dynamics of the metal ion–methane system

Non-adiabatic interactions are of great importance in chemical dynamics, often controlling the competitive branching between accessible channels in organometallic photochemistry. Photodissociation half-collision studies in small bimolecular complexes systems can serve as model systems for developing and enhancing our chemical intuition and as test cases for evaluating *ab-initio* structure calculations and theoretical molecular dynamics models. The photodissociation spectroscopy of weakly bound bimolecular complexes has proven to be an invaluable tool for probing and elucidating metal ion–hydorcarbon chemistry, and we look forward to even more dramatic progress in the coming years.

Acknowledgements

We are indebted to our colleagues and students who are largely responsible for the success of the work that we have described here: L. N. Ding, Y. C. Cheng, T. H. Wong, K. M. Montgomery, M. A. Young, A. M. Lyyra, K. M. Sando and W. C. Stwalley. We also gratefully acknowledge many helpful discussions with M. A. Duncan, W. H. Breckenridge and C. W. Bauschlicher, Jr. Our research has been carried out with generous support from the National Science Foundation and from the Donors to the Petroleum Research Fund of the American Chemical Society.

References

[1] Levy, D. H., 1981, *Adv. chem. Phys.*, **47**, 323.
[2] Janda, K. C., 1985, *Adv. chem. Phys.*, **60**, 201.
[3] Shin, S. K., Chen, Y., Nickolaisen, S., Sharpe, S. W., Beaudet, R. A., and Wittig, C., 1991, *Adv. Photochem* **16**, 249.
[4] (a) Breckenridge, W. H., Jouvet, C., and Soep, B., 1986, *J. chem. Phys.*, **84**, 1443; (b) Breckenridge, W. H., Jouvet, C., and Soep, B., 1995, *Advances in Metal Semiconductor Clusters*, Vol. III (New York: JAI Press), p. 1.
[5] Jouvet, C., Bovineau, M., Duval, M. C., and Soep, B., 1987, *J. phys. Chem.*, **91**, 5416.
[6] Takayanagi, M., and Hanazaki, I., 1991, *Chem. Rev.*, **91**, 1193.
[7] Zewail, A. H., 1991, *Faraday Discuss. chem. Soc.*, **91**, 207.
[8] Vaida, V., Donaldson, D. J., Sapers, S. P., Naaman, R., and Child, M. S., 1989, *J. chem. Phys.*, **93**, 513.
[9] Syage, J., 1996, *Chem. Phys.*, **206**, 411.
[10] King, D. S., Sauder, D. G., and Cassasa, M. P., 1994, *J. chem. Phys.* **100**, 4200.
[11] Herwitz, Y., and Naaman, R., 1995, *J. chem. Phys.*, **102**, 1941.
[12] Loomis, R. A., Schwartz, R. L., and Lester, M. I., 1996, *J. chem. Phys.*, **104**, 6984.
[13] Bernstein, E. R., 1992, *J. phys. Chem.*, **96**, 10105.
[14] Gotch, A. J., and Zwier, T. S., 1990, *J. chem. Phys.*, **93**, 6977; Garrett, A. W., and Zwier, T. S., 1992, *J. chem. Phys.*, **96**, 7259.
[15] Bowers, M. T., 1989, *Ion and Cluster-Ion Spectroscopy and Structure*, edited by J. P. Maier (New York: Elsevier), p. 241.
[16] (a) Castleman, A. W., Jr, and Wei, S., 1994, *Annu. Rev. phys. Chem.*, **45**, 685; (b) Keesee, R. G., and Castleman, A. W., Jr. *Ion and Cluster-Ion Spectroscopy and Structure*, edited by J. P. Maier (New York: Elsevier), p. 275.

[17] Hall, G. E., and Houston, P. L., 1989, *Annu. Rev. phys. Chem.*, **40**, 375.
[18] (a) Papanikolas, J. M., Vorsa, V., Nadal, M. E., Campagnola, P. J., Buchenau, H. K., and Linberger, W. C., 1993, *J. chem. Phys.*, **99**, 8733; (b) Nadal, M. E., Kleiber, P. D., and Lineberger, W. C., 1996, *J. chem. Phys.*, **105**, 504.
[19] (a) Buntine, M. A., Lavrich, D. J., Dessent, C. E., Scarton, M. G., and Johnson, M. A., 1992, *Chem. Phys. Lett.* **216**, 471; (b) Posey, L. A., and Johnson, M. A., 1988, *J. chem. Phys.* **89**, 4807.
[20] Chol, J. H., Kuwata, K. T., Haas, B. M., Cao, Y., Johnson, M. S., and Okamura, M., 1994, *J. chem. Phys.*, **100**, 7153.
[21] (a) Selegue, T. J., Moe, N., Draves, J. A., and Lisy, J. M., 1992, *J. chem. Phys.*, **96**, 7268; (b) Selegue, T. J., and Lisy, J. M., 1996, *J. chem. Phys.*, **105**, 2938.
[22] (a) Freiser, B. S., 1994, *Accts. Chem. Res.*, **27**, 353; (b) Afzaal, S., and Freiser, B. S., 1993, *Chem. Phys. Lett.*, **218**, 254; (c) Roth, L. M. and Freiser, B. S., 1991, *Mass Spectrom. Rev.*, **10**, 303.
[23] Burns, T. D., Spence, T. G., Mooney, M. A., and Posey, L. A., 1996, *Chem. Phys. Lett.*, **258**, 669.
[24] (a) Lessen, D. E., Asher, R. L., and Brucat, P. J., 1991, *J. chem. Phys.*, **95**, 1414; (b) Bellert, D. Buthelezi, T., Lewis, V., Dezfulian, K., and Brucat, P. J., 1995, *Chem. Phys. Lett.*, **246**, 145; (c) Lessen, D. E., Asher, R. L., and Brucat, P. J., 1983, *Advances in Metal and Semiconductor Clusters*, Vol. I, edited by M. A. Duncan (Greenwich, CT, JAI Press), p. 267; (d) Asher, R. L., Bellert, D., Buthelezi, T., Lessen, D. E., and Brucat, P. J., 1995, *Chem. Phys. Lett.*, **234**, 119; (e) Asher, R. L., Bellert, D., Buthelezi, T., and Brucat, P. J., 1994, *Chem. Phys. Lett.*, **227**, 277, 623; (f) Asher, R. L., Bellert, D., Buthelezi, T., Weerasekara, G., and Brucat, P. J., 1994, *Chem. Phys. Lett.*, **228**, 390; (g) Asher, R. L., Bellert, D., Buthelezi, T., and Brucat, P. J., 1995, *J. phys. Chem.*, **99**, 1068.
[25] (a) Misaizu, F., Sanekata, M., Tsukamoto, K., Fuke, D., and Iwata, S., 1992, *J. phys. Chem.*, **96**, 8259; (b) Misaizu, F., Sanekata, M., and Fuke, K., 1994, *J. chem. Phys.*, **100**, 1161; (c) Sanekata, M., Misaizu, F., Fuke, K., Iwata, S., and Hashimoto, K., 1995, *J. Am. chem. Soc.*, **117**, 747.
[26] (a) Farrar, J. M., 1993, *Cluster Ions*, edited by C. Y. Ng, T. Baer and I. Powis (New York: Wiley), p. 243; (b) Donnelly, S. G. and Farrar, J. M., 1993, *J. chem. Phys.*, **98**, 5450; (c) Schmuttenmaer, C. A., Qian, J., Donnelly, S. G., DeLuca, M. J., Varley, D. F., DeLouise, L. A., Miller, R. J. D., and Farrar, J. M., 1993, *J. phys. Chem.*, **97**, 3077; (d) Shen, M. H., and Farrar, J. M., 1991, *J. chem. Phys.*, **94**, 3322; (e) Shen, M. H., and Farrar, J. M., 1989, *J. phys. Chem.*, **93**, 4386.
[27] Qian, J., Midley, A. J., Donnelly, S. G., Lee, J. I., and Farrar, J. M., 1995, *Chem. Phys. Lett.*, **244**, 414.
[28] (a) Yeh, C. S., Pilgrim, J. S., Willey, K. F., Robbins, D. L., and Duncan, M. A., 1994, *Int. Rev. phys. Chem.*, **13**, 231; (b) Duncan, M. A., 1997, *Annu. Rev. phys. Chem.*, **48**, 69; (c) Yeh, C. S., Willey, K. F., Robbins, D. L., and Duncan, M. A., 1994, *Int. J. Mass Spectrom. Ion Processes*, **131**, 307.
[29] (a) Pilgrim, J. S., Yeh, C. S., Robbins, D. L., Berry, K. R., and Duncan, M. A., 1994, *J. chem. Phys.*, **100**, 7945; (b) Scurlock, C. T., Pilgrim, J. S., and Duncan, M. A., 1995, *J. chem. Phys.*, **103**, 3293; (c) Pullins, S. H., Scurlock, C. T., Reddic, J. E., and Duncan, M. A., 1996, *J. chem. Phys.*, **104**, 7518.
[30] Robbins, D. L., Brock, L. R., Pilgrim, J. S., and Duncan, M. A., 1995, *J. chem. Phys.*, 102, 1481.
[31] (a) Yeh, C. S., Willey, K. F., Robbins, D. L., and Duncan, M. A., 1992, *J. phys. Chem.*, **96**, 7833; (b) Yeh, C. S., Willey, K. F., Robbins, D. L., and Duncan, M. A., 1993, *J. chem. Phys.*, **98**, 1867; (c) Scurlock, C. T., Pullins, S. H., and Duncan, M. A., 1997, *J. chem. Phys.*, **105**, 3579.
[32] (a) Willey, K. F., Cheng, P. Y., Taylor, T. G., Bishop, M. B., and Duncan, M. A., 1990, *J. phys. Chem.*, **94**, 4769; (b) Willey, K. F., Cheng, P. Y., Bishop, M. B., and Duncan, M. A., 1991, *J. Am. chem. Soc.*, **113**, 4721; (c) Willey, K. F., Yeh, C. S., Robbins, D. L., and Duncan, M. A., 1992, *J. phys. Chem.*, **96**, 9106.
[33] Ding, L. N., Kleiber, P. D., Young, M. A., Stwalley, W. C., and Lyyra, A. M., 1993, *Phys. Rev.* A, **48**, 2024.

[34] (a) DING, L. N., KLEIBER, P. D., CHENG, Y. C., YOUNG, M. A., STWALLEY, W. C., and ONEIL, S. V., 1995, *J. chem. Phys.*, **102**, 5253; (b) DING, L. N., KLEIBER, P. D., YOUNG, M. A., and STWALLEY, W. C., 1993, *Chem. Phys. Lett.*, **212**, 499.
[35] CHEN, J., CHENG, Y. C., and KLEIBER, P. D., 1997, *J. chem. Phys.*, **106**, 77.
[36] CHENG, Y., CHEN, J., YOUNG, M. A., and KLEIBER, P. D., 1997, *J. chem. Phys.*, **107**, 3758.
[37] (a) DING, L. N., YOUNG, M. ., KLEIBER, P. D., STWALLEY, W. C., and LYYRA, A. M., 1993, *J. phys. Chem.*, **97**, 2181; (b) DING, L. N., 1994, PhD Thesis, University of Iowa.
[38] CHENG, Y. C., CHEN, J., DING, L. N., KLEIBER, P. D., and LIU, D. K., 1996, *J. chem. Phys.*, **104**, 6452.
[39] CHEN, J., CHENG, Y. C., and KLEIBER, P. D., 1997, *J. chem. Phys.*, **106**, 3884.
[40] CHEN, J., WONG, T. H., and KLEIBER, P. D., 1997, *Chem. Phys. Lett.* (to be published).
[41] CHEN, J., WONG, T. H., MONTGOMERY, K., and KLEIBER, P. D., 1997, *J. chem. Phys.* (to be published).
[42] ELLER, K., and SCHWARTZ, H., 1989, *Gas Phase Inorganic Chemistry*, edited by D. H. Russel (New York: Plenum); 1991, *Chem. Rev.*, **91**, 1121; 1996, *Organometallic Ion Chemistry*, edited by B. S. Frieser (Amsterdam: Kluwer).
[43] (a) HERTEL, I. V., 1982, *Adv. chem. Phys.*, **50**, 475; (b) HERTEL, I. V., 1982, *Dynamics of the Excited State*, edited by K. P. Lawley (New York: Wiley), p. 475.
[44] BRECKENRIDGE, W. H., 1996, *J. phys. Chem.*, **100**, 14840.
[45] FERRAUDI, G., 1988, *Elements of Inorganic Photochemistry* (New York: Wiley–Interscience).
[46] FREI, H., BLATTER, F., and SUN, H., 1996, *Chemtech*, **6**, 24.
[47] CORNETT, D. S., PESCHKE, M., LAIHING, K., CHENG, P. Y., WILLEY, K. F., and DUNCAN, M. A., 1992, *Rev. scient, Instrum.*, **63**, 2177.
[48] JOHNSON, M. A., and LINEBERGER, W. C., 1988, *Techniques for the Study of Ion–Molecule Reactions*, edited by J. M. Farrar and W. Saunders, Jr (New York: Wiley), p. 591.
[49] DIETZ, T. G., DUNCAN, M. A., POWERS, M. A., and SMALLEY, R. E., 1981, *J. chem. Phys.*, **74**, 6511.
[50] WILEY, W. C., and MCLAREN, I. H., 1955, *Rev. scient. Instr.* **26**, 1150.
[51] ALEXANDER, M. L., LEVINGER, N. E., JOHNSON, M. A., RAY, D. W., and LINEBERGER, W. C., 1988, *J. chem. Phys.*, **88**, 6200.
[52] KINSEY, J. L., 1977, *J. chem. Phys.*, **66**, 2560.
[53] PENN, S. M., HAYDEN, C. C., CARLSON, MUYSKENS, K. J., and CRIM, F. F., 1988, *J. chem. Phys.*, **89**, 2090.
[54] HUANG, Y., HE, G., YANG, Y., HASHIMOTO, S., and GORDON, R. J., 1994, *Chem. Phys. Lett.*, **229**, 621.
[55] NAGATA, T., and KONDOW, T., 1993, *J. chem. Phys.*, **98**, 290.
[56] (a) HWANG, H. J., and EL-SAYED, M. A., 1991, *J. chem. Phys.* **94**, 4877; (b) HWANG, H. J., PhD Thesis, University of California, Los Angeles, 1991.
[57] BAUSCHLICHER, C. W., JR, 1993, *Chem. Phys. Lett.*, **201**, 11.
[58] CHEN, J., and KLEIBER, P. D., 1997, unpublished work.
[59] (a) TRUHLAR, D. G., DUFF, J. W., BLAIS, N. C., TULLY, J. C., and GARRETT, B. C., 1982, *J. chem. Phys.*, **77**, 764; (b) HALVICK, P., and TRUHLAR, D. G., 1992, *J. chem. Phys.*, **96**, 2895; (c) SCHWENK, D. W., MIELKE, S. L., TAWA, G. J., FRIEDMAN, R. S., HALVICK, P., and TRUHLAR, D. G., 1993, *Chem. Phys. Lett.*, **203**, 565.
[60] BOTSCHWINA, P., MEYER, W., HERTL, I. V., and REILAND, W., 1981, *J. chem. Phys.*, **75**, 5438.
[61] BRECKENRIDGE, W. H., and UMEMOTO, H., 1984, *J. chem. Phys.*, **80**, 4168.
[62] (a) ADAMS, N., BRECKENRIDGE, W. H., and SIMONS, J., 1981, *Chem. Phys.*, **56**, 327; (b) CHAQUIN, P., SEVIN, A., and YU, H., 1985, *J. chem. Phys.*, **89**, 2813.
[63] KLEIBER, P. D., LYYRA, A. M., SANDO, K. M., ZAFIROPULOS, V., and STWALLEY, W. C., 1986, *J. chem. Phys.*, **85**, 5493.
[64] (a) BILILIGN, S., and KLEIBER, P. D., 1992, *J. chem. Phys.*, **96**, 213; (b) BILILIGN, S., KLEIBER, P. D., KEARNEY, W. R., and SANDO, K. M., 1992, *J. chem. Phys.*, **96**, 218.
[65] (a) KLEIBER, P. D., 1996, *Chemical Dynamics and Kinetics of Small Radicals*, edited by K. Liu and A. Wagner (Singapore: World Scientific), p. 573; (b) KLEIBER, P. D., STWALLEY, W. C., and SANDO, K. M., 1993, *Annu. Rev. phys. Chem.*, **44**, 13.

[66] WALLACE, I., FUNK, D. J., KAUP, J. G., and BRECKENRIDGE, W. H., 1992, *J. chem. Phys.*, **97**, 3135.
[67] (a) BRECKENBRIDGE, W. H., and UMEMOTO, H., 1982, *The Dynamics of the Excited State*, edited by K. Lawley (New York: Wiley); (b) BRECKENRIDGE, W. H., 1983, *Reactions of Small Transient Species*, edited by M. Clyne and A. Fontijin (London: Academic Press), p. 157.
[68] SIEGBAHN, P. E. M., SVENSSON, M., and CRABTREE, R. H., 1995, *J. Am. chem. Soc.*, **117**, 6758.
[69] LOW, J. J., and GODDARD, W. A., 1984, *J. Am. chem. Soc.*, **106**, 8321.
[70] BAUSCHLICHER, C. W., and SODUPE, M., 1993, *Chem. Phys. Lett.*, **214**, 489.
[71] BRECKENRIDGE, W. H., and UMEMOTO, H., 1981, *J. chem. Phys.*, **75**, 698; 1982, *ibid.*, **77**, 4464.
[72] WONG, T. H., and KLEIBER, P. D., 1995, *J. chem. Phys.*, **102**, 6476.
[73] CHAQUIN, P., PAPAKONDYLIS, A., GIESSNER-PRETTRE, C., and SEVIN, A., 1990, *J. phys. Chem.*, **94**, 7352.
[74] LIU, D. K., OU, Y. R., and LIN, K. C., 1996, *J. chem. Phys.*, **104**, 1370.
[75] HERZBERG, G., 1966, *Molecular Spectra and Molecular Structure: Spectra of Polyatomic Molecules*, Vol. III (New York: Van Nostrand Reinhold).
[76] WALLACE, I., and BRECKENRIDGE, W. H., 1992, *J. chem. Phys.*, **97**, 2318.
[77] BAUSCHLICHER, C. W., and PARTRIDGE, J., 1991, *J. phys. Chem.*, **95**, 3946.
[78] BAUSCHLICHER, C. W., SODUPE, M., and PARTRIDGE, J., 1992, *J. chem. Phys.*, **96**, 4453.
[79] MULLIKEN, R. S., 1952, *J. Am. chem. Soc.*, **64**, 811.
[80] SODUPE, M., and BAUSCHLICHER, C. W., 1994, *Chem. Phys. Lett.*, **185**, 163.
[81] REID, C., 1950, *J. chem. Phys.*, **18**, 1299.
[82] MERER, A. J., and MULLIKEN, R. S., 1969, *Chem. Rev.*, **69**, 639.